AIR FORCE INSTITUTE OF TECHNOLOGY

AIR UNIVERSITY
UNITED STATES AIR FORCE

SCHOOL OF ENGINEERING

WRIGHT–PATTERSON AIR FORCE BASE, OHIO

GEP/PH/72-12

LOCK-ON RANGES OF LASER-GUIDED SYSTEMS

THESIS

GEP/PH/72-12 JAMES V. MARDIS
CAPTAIN USAF

Ia

UNCLASSIFIED

Security Classification

DOCUMENT CONTROL DATA - R & D

(Security classification of title, body of abstract and indexing annotation must be entered when the overall report is classified)

1. ORIGINATING ACTIVITY (Corporate author)

Air Force Institute of Technology (AFIT-EN)
Wright-Patterson AFB, Ohio 45433

2a. REPORT SECURITY CLASSIFICATION: Unclassified

2b. GROUP:

3. REPORT TITLE

LOCK-ON RANGES OF LASER-GUIDED SYSTEMS

4. DESCRIPTIVE NOTES (Type of report and inclusive dates)

AFIT Thesis

5. AUTHOR(S) (First name, middle initial, last name)

James V. Mardis
Captain, USAF

6. REPORT DATE	7a. TOTAL NO. OF PAGES	7b. NO. OF REFS
June 1972	95	42

8a. CONTRACT OR GRANT NO.	9a. ORIGINATOR'S REPORT NUMBER(S)
b. PROJECT NO.	GEP/PH/72-12
c.	9b. OTHER REPORT NO(S) (Any other numbers that may be assigned this report)
d.	

10. DISTRIBUTION STATEMENT

Approved for Public Release. Distribution Unlimited

Approved for public release; IAW AFR 190-17
Keith A. Williams, 1st Lt., USAF
Acting Director of Information

12. SPONSORING MILITARY ACTIVITY

Operations Evaluation Group (HQ USAF - SAV)
Assistant Chief of Staff, Studies & Analysis
HQ USAF, Pentagon

13. ABSTRACT

This thesis is an evaluation of the factors that determine the maximum acquisition and tracking (lock-on) range of laser-guided systems in the military close-air-support mission. The problem is divided into a study of the designed system parameters which are characterized by a clear-air lock-on range, and a study of the effect of the intervening atmosphere. Three model atmospheres are considered: a homogeneous, an exponential, and a three-layer stratified atmospheric aerosol vertical structure. The vertical aerosol number density distribution of a real atmosphere can be bracketed between a homogeneous and an exponential atmospheric model. Conversion charts from clear-air lock-on range to actual lock-on range for the three model atmospheres are plotted. It was found that beamspreading by aerosols can be large for moderate attenuation coefficients. Reflective cross sections of a jeep model were found to have a standard deviation of ±20% of the mean for two olive drab paints. Attenuation coefficients at 1.065 microns are determined for atmospheric gases and rain. A method is presented for determining aerosol attenuation at 1.065 microns from the visibilities measured through red and blue filters; comparison of this method with the computer analysis by others was successful but experimental tests were inconclusive due to equipment and weather problems.

IR

DD FORM 1 NOV 65 1473

UNCLASSIFIED

Security Classification

14. KEY WORDS	LINK A		LINK B		LINK C	
	ROLE	WT	ROLE	WT	ROLE	WT
Lasers						
Laser-guided systems						
Aerosols						
Atmospheric Attenuation						
Weather attenuation						
Laser beams						
Reflectance						
Aerosol Attenuation						
Atmospheric structure						
Visibility						

II k

GEP/PH/72-12

LOCK-ON RANGES OF LASER-GUIDED SYSTEMS

THESIS

Presented to the Faculty of the School of Engineering
of the Air Force Institute of Technology

Air University
in Partial Fulfillment of the
Requirements of the Degree of

Master of Science

by

James V. Mardis, B.S.
Captain USAF

Graduate Engineering Physics

June 1972

Preface

This thesis is the conclusion of my investigation into the factors that affect the lock-on range of laser-guided systems in the close-air-support mission. It is a summary of the elements of a complex and important operational problem, an analysis of areas where knowledge is lacking, and a presentation of some methods of solution of specific problems in these deficient areas. There is no classified information here: all items in this report are my own or come from unclassified and commonly available sources.

The assistance of the following persons is gratefully acknowledged: Bob Maxwell, Jerry Beard, Bill Malila, and Bob Turner of the University of Michigan; Dr. Robert Fenn of the AF Cambridge Research Labs; Dr. Ken Jungling of AFIT; Dr. Elias Reisman of Philco-Ford; Barry Hogge, Walter Visinsky, Lt. Col. S.F. Johnston, David Shivell, Ron Nelson, Bob Endlich, and Dick Delay of the AF Weapons Lab; Jim Rachal, Ron Hubbard, Dick Firsdon, Hal Watson, and Don Matulka of the AF Avionics Lab. I also greatly appreciate the excellent advice, close cooperation, and meaningful discussions with my two advisors: Dr. Leno Pedrotti, Head of the Physics Department, AFIT, and Colonel Ed Battle, Chief, Operations Evaluation Group, Assistant Chief of Staff, Studies and Analysis, Pentagon.

But my greatest appreciation goes to my wonderful family; without their loving understanding of the situation this study of such an extensive problem would have been greatly limited. I now have a great debt of time, attention, and affection to repay to my loving, patient wife Diane and my loving, usually impatient, 9-month-old daughter Jill.

Contents

Contents

List of Figures

List of Figures

List of Tables

Abstract

This thesis is an evaluation of the factors that determine the maximum acquisition and tracking (lock-on) range of laser-guided systems in the military close-air-support mission. The problem is divided into a study of the designed system parameters which are characterized by a clear-air lock-on range, and a study of the effect of the intervening atmosphere. Three model atmospheres are considered: a homogeneous, an exponential, and a three-layer stratified atmospheric aerosol vertical structure. The vertical aerosol number density distribution of a real atmosphere can be bracketed between a homogeneous and an exponential atmospheric model. Conversion charts from clear-air lock-on range to actual lock-on range for the three model atmospheres are plotted. It was found that beamspreading by aerosols can be large for moderate attenuation coefficients. Reflective cross sections of a jeep model were found to have a standard deviation of $\pm$20% of the mean for two olive drab paints. Attenuation coefficients at 1.065 microns are determined for atmospheric gases and rain. A method is presented for determining aerosol attenuation at 1.065 microns from the visibilities measured through red and blue filters; comparison of this method with the computer analysis by others was successful but experimental tests were inconclusive due to equipment and weather problems.

GEP/PH/72-12

LOCK-ON RANGES OF LASER-GUIDED SYSTEMS

I. Introduction

Background

The purpose of this study is to investigate the factors that determine the lock-on range of laser-guided systems in the military close-air-support mission.

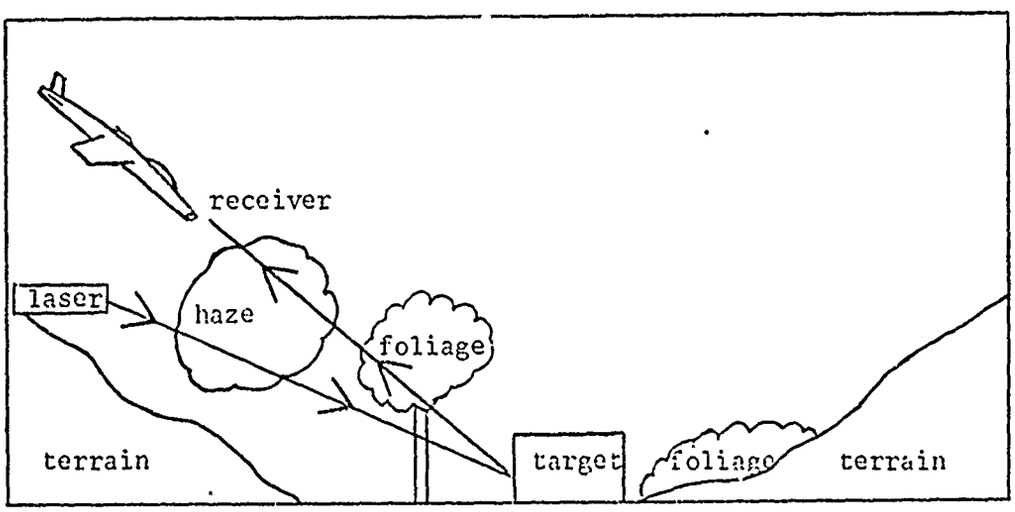

Fig. 1. Diagram of a Laser-guided System

A laser beam is used to illuminate a target as in Figure 1. The reflected laser energy is detected by a narrowband electro-optical receiver and used to guide the receiver to the target. The maximum range at which the receiver can acquire and track the target (lock-on range) is limited by the laser power, beam divergence, target reflective characteristics, receiver sensitivity, and the atmosphere in the path.

Atmospheric attenuation is a severely limiting factor in the operational employment of laser-guided systems, since the useful lock-on range may be reduced by a factor of 20 in weather that a pilot can still fly by visual references. Certain laser wavelengths such as 1.065 microns (μ) have better propagation characteristics than those in the visual range, due to less scattering and absorption. In adverse weather,

attenuation at 1.065 μ is principally due to scattering by liquid water aerosols, plus slight absorption from water vapor and from dust aerosols. Prediction of attenuation in a real atmosphere is beyond the state of the art, as is prediction of the reflective characteristics of a complex target in a combat environment. Finally, there is very little standardization in the literature regarding laser beam divergence definitions, reflectance terminology and characteristics, and atmospheric transmittance terminology and characteristics.

The solution of this problem is of interest to the Operations Evaluation Group (USAF-SAV) of the Air Staff. In the presentation of this problem, they instructed the researcher to:

1. Determine what factors most severely limit the maximum lock-on range of laser-guided systems in adverse weather.
2. Propose improvements to increase the lock-on range.
3. Comment on factors that may affect the tactics or operational employment of these systems, but keep the written thesis unclassified.

Scope

Important sub-problems are beam characteristics, beam-target geometry, target reflectance, receiver characteristics, attenuating mechanisms, aerosol composition and size distribution, atmospheric vertical profile models, real atmospheres, statistical variation in lock-on ranges, and methods of approximating values of aerosol attenuation. The tasks are to determine the state of the art, identify areas where knowledge is lacking, evaluate the relative importance of these areas, propose solutions, and test these proposals experimentally or by computer analysis.

Limitations and Assumptions

This thesis is limited to an analysis of 1.065-μ laser systems at ranges of 0.5 - 10 Km. Nonlinear effects and optical countermeasures are not considered. It is assumed that beam wander is either compensated for in laser pointing and tracking or is negligible. It is assumed that the human (photopic) eye can detect a 2% contrast through narrowband filters anywhere in the visual range as well as with white light.

Organization

The clear-air lock-on range due to system geometry will be determined in Chapter Two. Beam, target, and receiver characteristics will be discussed as they apply to the operational problem. Chapter Three will evaluate the attenuation of laser beams by gases and aerosols in model and real atmospheres. A method for determining attenuation coefficients from meteorological measurements will be presented and evaluated. In Chapter Four the clear-air lock-on range will be combined with three different model atmospheres to yield a true lock-on range. The statistical variation in this true lock-on range will be discussed. Chapter Five will test and evaluate one of the proposals to determine the attenuation coefficients from meteorological range measurements through narrowband filters. The major conclusions and recommendations are given in Chapter Six.

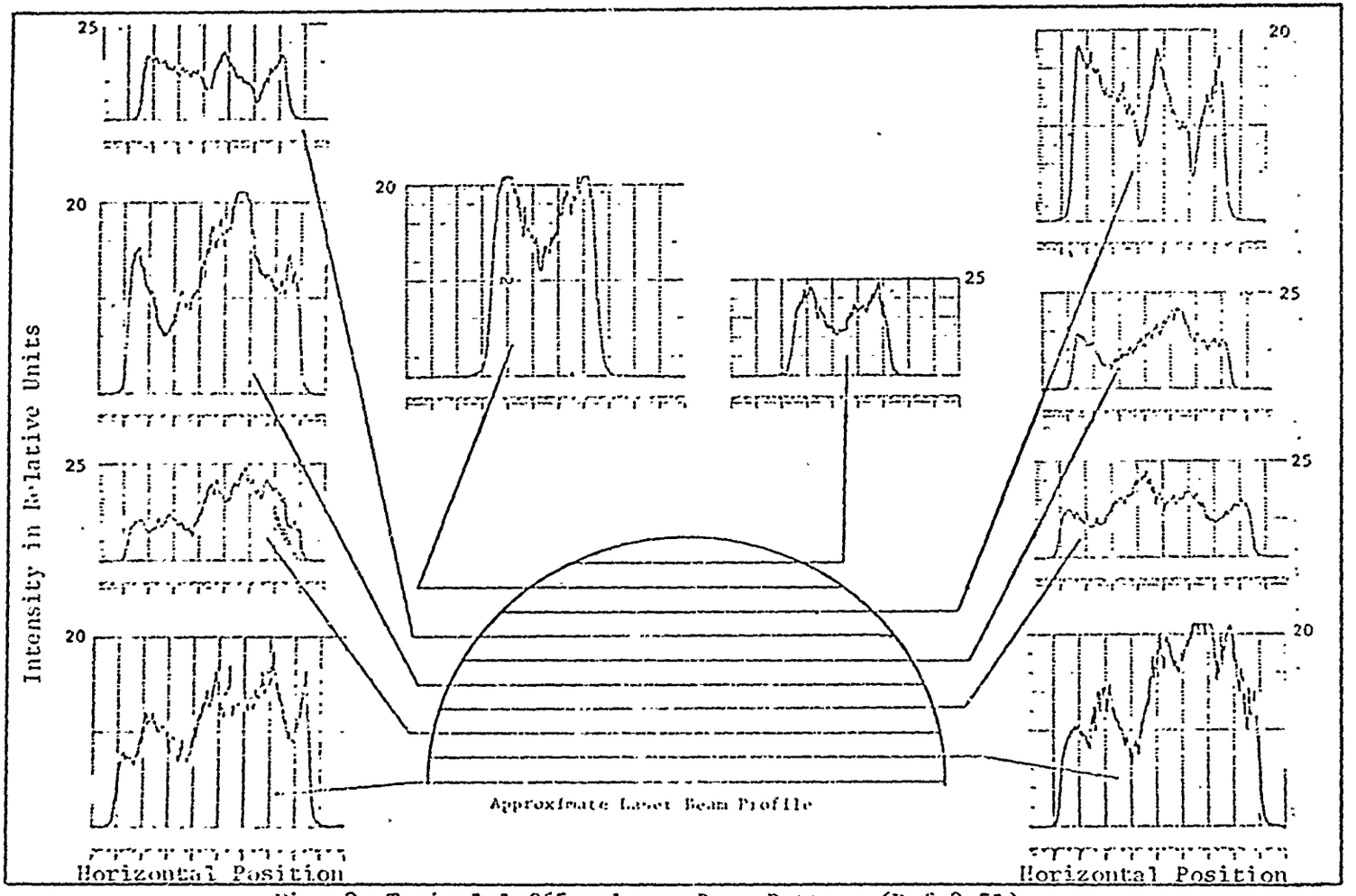

Fig. 2. Typical 1.065 μ Laser Beam Pattern (Ref 2:51)

II. Geometry of the Illuminator-Target-Receiver Problem

Characteristics of the Laser Beam

Military laser specifications require a beam with a gaussian intensity profile across the beam. This may be achieved in systems with electrically polarizing cells as the Q-switch, but is almost impossible to achieve in systems that use a rotating mirror as the Q-switch. The latter device almost always results in a multi-mode lasing action, with highly irregular and erratic intensity distribution across the beam. The difference in beam pattern is mostly of academic and computational interest, as scintillation in the atmosphere will often cause far more serious disturbances to the beam's internal structure.

The computational problems involved in a multi-mode beam can be immediately understood by observing Figure 2, a series of cross-sectional sweeps across a military 1.065-μ laser beam by the Target Signatures Analysis Center (TSAC), University of Michigan (Ref 2:51). If several pulses are averaged together, the irregularities in the intensity distribution average out, so for many practical cases an assumption of constant illumination across the beam is better than an assumption of a gaussian distribution. This report will consider two cases of laser beam profiles: a gaussian and a constant average intensity (irradiance) distribution across the beam, thus covering most practical cases. Detection warning and countermeasures receivers, however, can respond to the peak pulse intensity.

The constant average illumination beam is defined by:

$$I(r) = I(o) \qquad \text{for } r \leq w$$
$$I(r) = 0 \qquad \text{for } r > w \tag{1}$$

The general definition of a gaussian intensity distribution is:

$$\frac{I(r)}{I(o)} = \frac{c}{\pi w^2} e^{-c\left(\frac{r}{w}\right)^2} \qquad (2)$$

where:

r = radius from the center of the beam pattern, in cm.
w = a defined half-width of the beam pattern, in cm.
c = a scale constant depending on the definition of w (see Table I).
c = 2.3026 for the standard definition used in this thesis.
I(r) = irradiance at radius r in the beam pattern, in watts/cm^2
I(o) = irradiance at the center of the beam pattern, in watts/cm^2.
$\frac{c}{\pi w^2}$ = a height-normalizing constant such that $\int_S \frac{I(r)}{I(o)} dS = 1$.
S = integrating surface across the beam through r,w.

There are several means of specifying whole-angle beam divergences of a gaussian laser beam in the optical far field. All appear with nearly equal frequency in military laser illuminator specifications without much consistency or clarification about which method is used. In more recent reports and specifications the beam divergence is most commonly defined as the cone containing 90% of the total beam energy. This thesis will follow this convention. Of all the definitions used, this results in the narrowest real beam for a given numerical divergence.

Beam divergences are sometimes defined by the cone containing 50% of the beam energy; or, by the cone at the points where the local intensity becomes 10%, 50%, 1/e, 1/e^2, -10 dB, or -3 dB of the intensity at the beam axis. Caution must be used to determine which definition of beam divergence is used with which laser illuminator. A computer program was developed (Appendix A) to compare all other definitions with the first. The results are in Table I.

Irradiance of the Target

Irradiance by the Laser Beam. Once the laser beam has reached the optical far field, the beam diameter can then be determined in the absence of atmospheric effects b,.

Table I

Comparison of Beam Divergence Definitions Frequently Used

If the whole-beam divergence angle is defined by:	At these points I(r)/I(o) =	Value of "c" in Eq (2) =	% of power contained in defined beam:	To convert to first definition, multiply the given angle by:
90% enclosed energy points	.1000	2.3026	90.00	1.000
90% intensity points	.1000	2.3026	90.00	1.000
-10 dB intensity points	.1000	2.3026	90.00	1.000
$1/e^2$ intensity points	.1353	2.0000	86.47	1.075
1/e intensity points	.3679	1.0000	63.21	1.517
1/2 enclosed energy points	.5000	0.6932	50.00	1.823
1/2 intensity points	.5000	0.6932	50.00	1.823
-3 dB intensity points	.5021	0.6908	49.88	1.826

$$d = 2R \text{ Tan } (\frac{\alpha}{2}) + d_o \qquad (3)$$

where:

α = beam divergence whole-angle in the far field.
R = illuminator - target range.
d = beam diameter in the far field at range R.
d_o = laser illuminator beam exit diameter (if this is in the far field) or the diameter of the rearward projection of the divergence angle to the laser exit window.

If $\alpha < 100$ milliradians, Eq (3) is approximated within 0.4% by:

$$d = \frac{R\alpha}{10} + d_o \quad (d, d_o \text{ in cm; R in meters; } \alpha \text{ in milliradians}) \qquad (4)$$

The power density (irradiance) in the beam is of considerable value in optical countermeasures design. Two cases are of primary interest: the constant average distribution and the gaussian distribution. In the absence of atmospheric effects, the former is given by:

$$H(r) = \frac{4P}{\pi d^2} = \frac{4P}{\pi(R\alpha + d_o)^2} \qquad (5)$$

where:

P = transmitter power.
d = beam diameter enclosing 100% of the constant beam energy.
H = irradiance at the target position in the beam.
α = whole-angle beam divergence at 100% enclosed-energy points.
d_o = beam exit diameter, as in Eq (3).

For a gaussian distribution, the irradiance at the target position is: (from Eq (2)):

$$H(r) = \frac{2.3026P}{\pi(\frac{d}{2})^2} e^{-2.3026[\frac{r^2}{(\frac{d}{2})^2}]} = \frac{9.2104P}{\pi d^2} e^{-9.2104(\frac{r}{d})^2} \qquad (6)$$

where:

d = beam diameter enclosing 90% of gaussian beam energy = $R\alpha + d_o$.
α = beam divergence whole-angle between 90% enclosed-energy points.
r = radial position normal to the beam at range R.
P, d_o, H, R as in Eq (5).

Irradiance by Other Sources. Of all the other sources of illumination of the target, the direct solar radiation is by far the

most intense. For a 100 Å window about 1.065 μ, at sea level on a clear day it is 3 - 6 watts/meter^2, depending on the solar zenith angle (Ref 37: 6-6,6-8). The average radiance of the scattered light from each corresponding solid angle of the clear daytime sky is 2×10^{-6} as strong as the radiance from the sun, at 1.065 μ (Ref 3:1314), but over the whole sky the total becomes 21% as much as the direct solar irradiance. Individual bright clouds may have a radiance up to ten times that of the background sky, but thicker, darker clouds may greatly attenuate the direct and indirect irradiance from the sun, so that the net contribution from clouds is unpredictable: it varies with the sun angle from the target and the angle from the target to each of the individual clouds.

The total day or night emission from sky or clouds at 1.065 μ is less than 10^{-3} as strong as the sky or cloud scattered light (Ref 3: 1314), and can be neglected. Thus the total daytime direct and indirect background irradiance onto the target is 3 - 8 watts/meter^2 (300 - 800 microwatts/cm^2) for a 100 Å window at 1.065 μ. This is a factor of 10^3 to 10^8 lower than the peak pulse illumination by most typical systems at reasonable target ranges.

Portion of the Beam Energy Intercepted by the Target

Since the beam at the target may be smaller or larger than the projected cross section of the target, it is necessary to compute what portion of the total beam energy is intercepted by the target. The remainder will be lost into the background, which usually has a higher reflectance and may be a significant distance behind the target. This results in two separated illumination and lock-on problems.

A computer program was created to determine the portion of the laser beam intercepted by targets of different shapes: round, square,

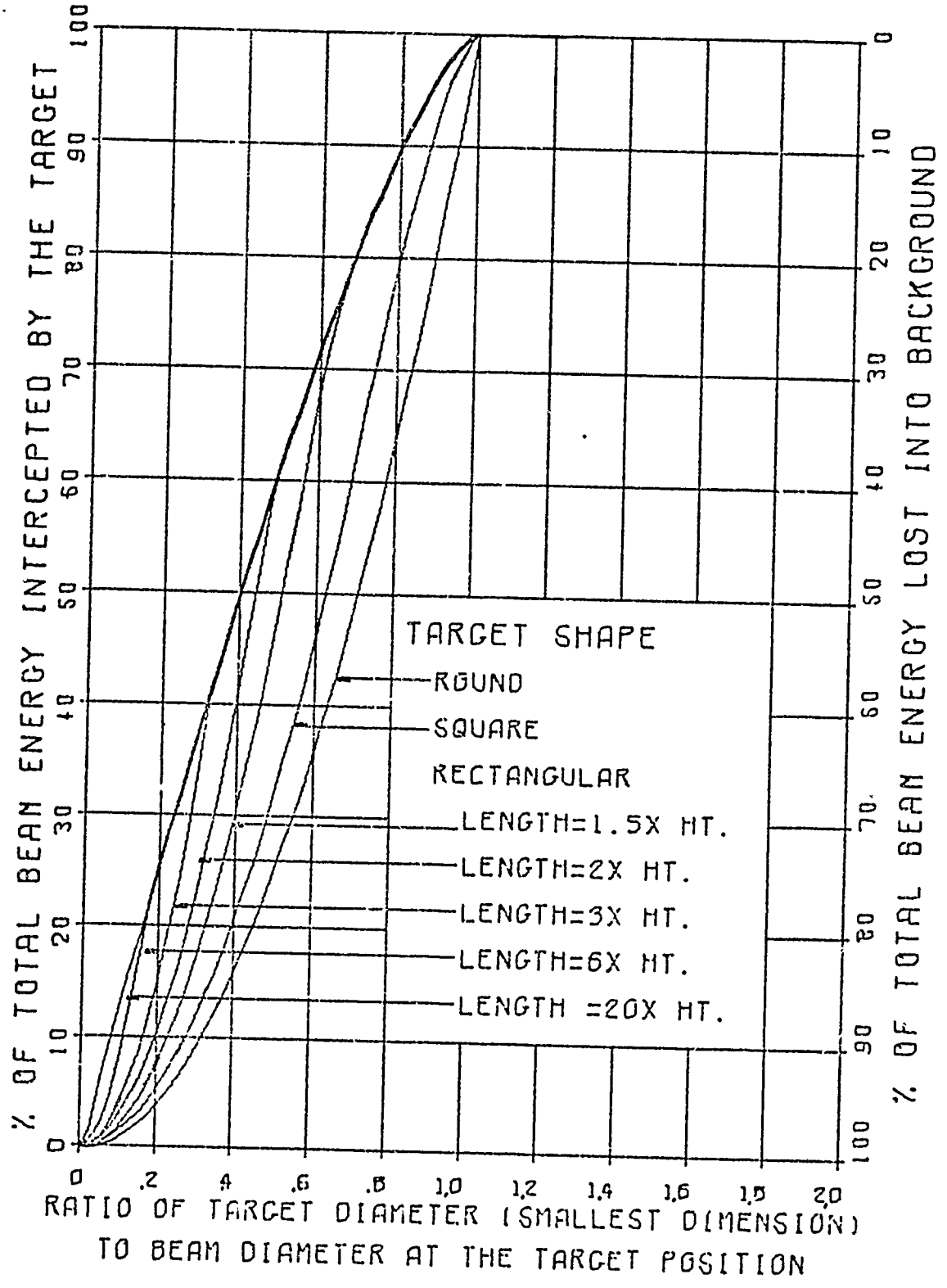

Fig. 3. Constant Beam Illuminating Targets of Different Shapes

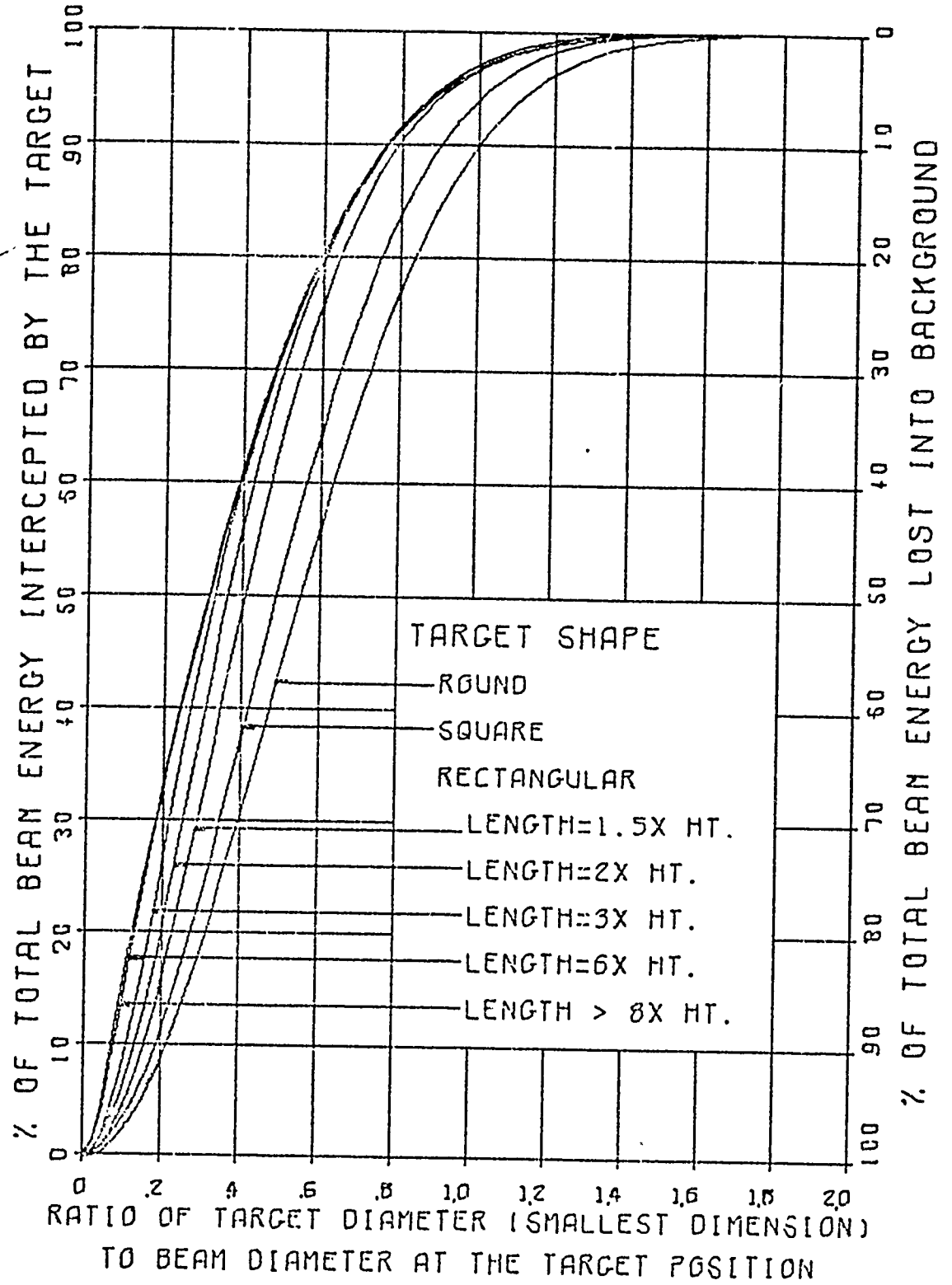

Fig. 4. Gaussian Beam Illuminating Targets of Different Shapes

and rectangular for length-to-height ratios of n = 1.5, 2, 3, 4, 5, 6, 8, 10, and 20; for a gaussian beam and a constant cross-section beam. The irradiance of Eqs (5) and (6) was integrated across the target shape and the results plotted in Figure 3 and Figure 4. The calculations are in Appendix B. In Figure 4 there was no visible change in the curve shape above n = 8.

Target Reflectance

A real surface can be considered to be covered with a broad size distribution of Mie scattering particles. The surface will have a relatively broad and strong forward scattering lobe (specular beam) and a general diffuse reflection in all directions, a result of summing the Mie reflection lobes of all the particles. The real surface will also have interference effects due to the surface fine structure (grain of wood, cloth) and polarization effects.

The term "reflectance" is frequently used synonymously with albedo, spectral reflectance, directional reflectance, bi-directional reflectance, reflection distribution function, and target reflectance cross section. It is so easy to misuse the published numerical values of these terms that a few words of caution and clarification are in order.

Albedo is usually the same as reflectance, the ratio of total radiant power reflected P_r to the total power incident P_i on a surface:

$$\rho = \frac{P_r}{P_i} \tag{7}$$

But albedo is sometimes used to include black-body emission. Spectral reflectance is the reflectance in a narrow band about a wavelength λ:

$$\rho_\lambda = \frac{P_{r\lambda}}{P_{i\lambda}} \tag{8}$$

Directional Reflectance is the ratio of the radiant power reflected into a specific solid angle, to the total power incident from all directions:

$$\rho_d \equiv \rho(\theta_r,\phi_r) \equiv \frac{P_r(\theta_r,\phi_r)}{P_i} = \frac{J(\theta_r,\phi_r)\, d\Omega}{P_i} \quad \text{for a body} \tag{9}$$

where:

$P_r(\theta_r,\phi_r)$ = power reflected into direction (θ_r,ϕ_r), in watts.
$J(\theta_r,\phi_r)$ = radiant intensity into direction (θ_r,ϕ_r), in watts/steradian.
$d\Omega$ = solid angle subtended by the small, distant receiver.

For a small target surface area dA_t, this becomes:

$$\rho_d \equiv \rho(\theta_r,\phi_r) = \frac{N_r(\theta_r,\phi_r)\, d\Omega\, dA_\perp}{H\, dA_t} = \frac{N_r(\theta_r,\phi_r)\, d\Omega \cos\theta_r}{H} \tag{10}$$

where:

H = irradiance onto the actual target area dA_t in watts/cm^2 of actual target area.

$$N_r(\theta_r,\phi_r) \equiv \frac{d^2 P_r(\theta_r,\phi_r)}{\cos\theta_r\, dA_t\, d\Omega} \equiv \text{radiance in watts/steradian-cm}^2 \text{ of projected area perpendicular } (A_\perp) \text{ to the line to the receiver.} \tag{11}$$

A very dusty surface is approximated reasonably well by a perfectly diffusing (Lambertian) surface ($N_r(\theta_r,\phi_r)$ = constant = N), so the total power reflected from a target surface area dA_t is:

$$\frac{dP_r}{dA_t} = \int_\Omega N \cos\theta\, d\Omega = \int_0^{2\pi}\int_0^{\frac{\pi}{2}} N \cos\theta \sin\theta\, d\theta\, d\phi = N\pi \tag{12}$$

For this very dusty surface the directional reflectance is:

$$\rho_d = \frac{\frac{dP_r}{dA_t}}{\frac{dP_i}{dA_t}} = \frac{\pi N}{H}, \text{ or } N = \frac{\rho_d H}{\pi} \quad \text{in watts/steradian-cm}^2 \text{ of projected area perpendicular to the line to the receiver.} \tag{13}$$

This "projected area" is either the projection of the illuminated target surface area onto a surface perpendicular to the line to the receiver ($A_t \cos\theta_r$), or the projected area that is within the field of view of

the receiver at that projected point, whichever is least. The irradiance H is the power onto the surface divided by the actual target surface area A_t, in watts/cm^2. It must be uniform and cover all of A_t, or A_t must be broken up into smaller elements. For a real, non-Lambertian surface N usually has a very strong angular dependence other than the cos θ_r dependence, and the directional reflectance of the surface $\rho_d = \frac{1}{H}\iint N(\theta_r,\phi_r) \cos\theta_r \sin\theta_r \, d\theta_r \, d\phi_r$ becomes very difficult to evaluate. ρ_d may be much greater than 1 at certain angles but will average out over all space to be 1 or less.

Bi-directional reflectance (partial reflectance) (reflectance distribution function) is the ratio of the radiant power reflected into a specific solid angle, to the radiant power incident from a specific solid angle. It is assumed that the incident power is collimated. The surface irradiance is therefore $H(\theta_i,\phi_i) = H_{beam}\cos\theta_i$. Similarly to the arguments for directional reflectance, there is for this geometry a bi-directional reflectance $\rho_p \equiv \rho(\theta_i,\phi_i,\theta_r,\phi_r)$ such that $\int \rho_p d\Omega = \rho_d$, where Ω is the influx or efflux hemisphere above the target surface. For a perfect Lambertian surface this becomes (Ref 27:117):

$$\rho_d = \rho_p \int d\Omega = \pi\rho_p \tag{14}$$

Therefore $N = \frac{\rho_d}{\pi} H$ becomes $N = \rho_p H$. For a real, non-Lambertian surface:

$$\rho_p = \frac{\iint N(\theta_r,\phi_r) \cos\theta_r \sin\theta_r \, d\theta_r \, d\phi_r}{H(\theta_i,\phi_i)} \tag{15}$$

where the integration limits are over the reflectance cone $d\theta_r \, d\phi_r$.

For a real surface ρ_p may be much greater than $\frac{1}{\pi}$ at certain angles but will average over all space to be $\frac{1}{\pi}$ or less. Integration of the receiver or source flux over the total hemisphere above the surface

yields the total reflected or incident radiation, respectively, and hence yields the directional reflectance ρ_d which is π times the average ρ_p: $\rho_d = \pi \bar{\rho}_p$. Integration of both source and receiver fluxes over the hemisphere above the surface yields the total reflectance ρ:

$$\rho = \bar{\rho}_d = \pi \bar{\rho}_p \tag{16}$$

The term "directional reflectance" is frequently and unfortunately used when an author means "bi-directional reflectance". The "bi" is implied.

Reflective Cross Section

There are two parts to the problem: target material and target geometry. The Target Signatures Analysis Center has measured, computed, or catalogued the spectral, directional, and bi-directional reflectances of several thousand materials of tactical interest. Their mathematical model for the bi-directional reflectance of a material consists of a weighted sum of three parts: one part perfectly diffuse reflection from a hard surface, one part perfectly specular reflection from a hard surface, and one part multiple diffuse volume reflection from a thin volume of scattering dielectrics on the surface (paint). The three parts are weighted according to theoretical and experimental data.

For a complex-shaped target such as a vehicle, the different surface materials at different angles results in a complicated total-target bi-directional cross section. For constant irradiance H:

$$\sigma_t \equiv \frac{J}{H} = \frac{1}{H} \int_{S=\text{Total vehicle surface}} \rho_p H \, dS \qquad \text{in} \quad \frac{\text{watts/steradian}}{\text{watts/}_{cm^2}} \tag{17}$$

TSAC has computed this function for a mathematical jeep model which was validated by field measurements. One set of their computations is in Figure 5, a polar logarithmic plot of the total-target reflective cross section σ_t for three receiver zenith angles. The specular peak

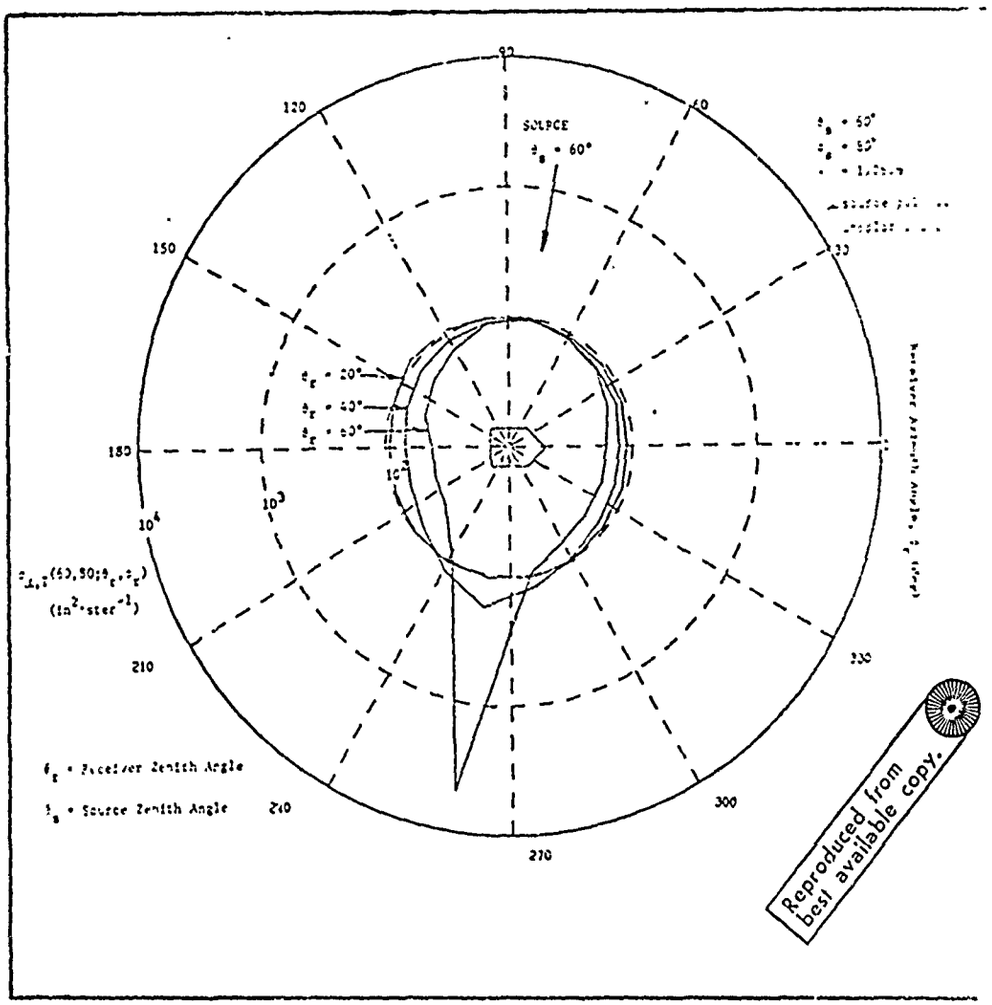

Fig. 5. Reflective Cross Sections for Jeep Model (Ref 2:5-

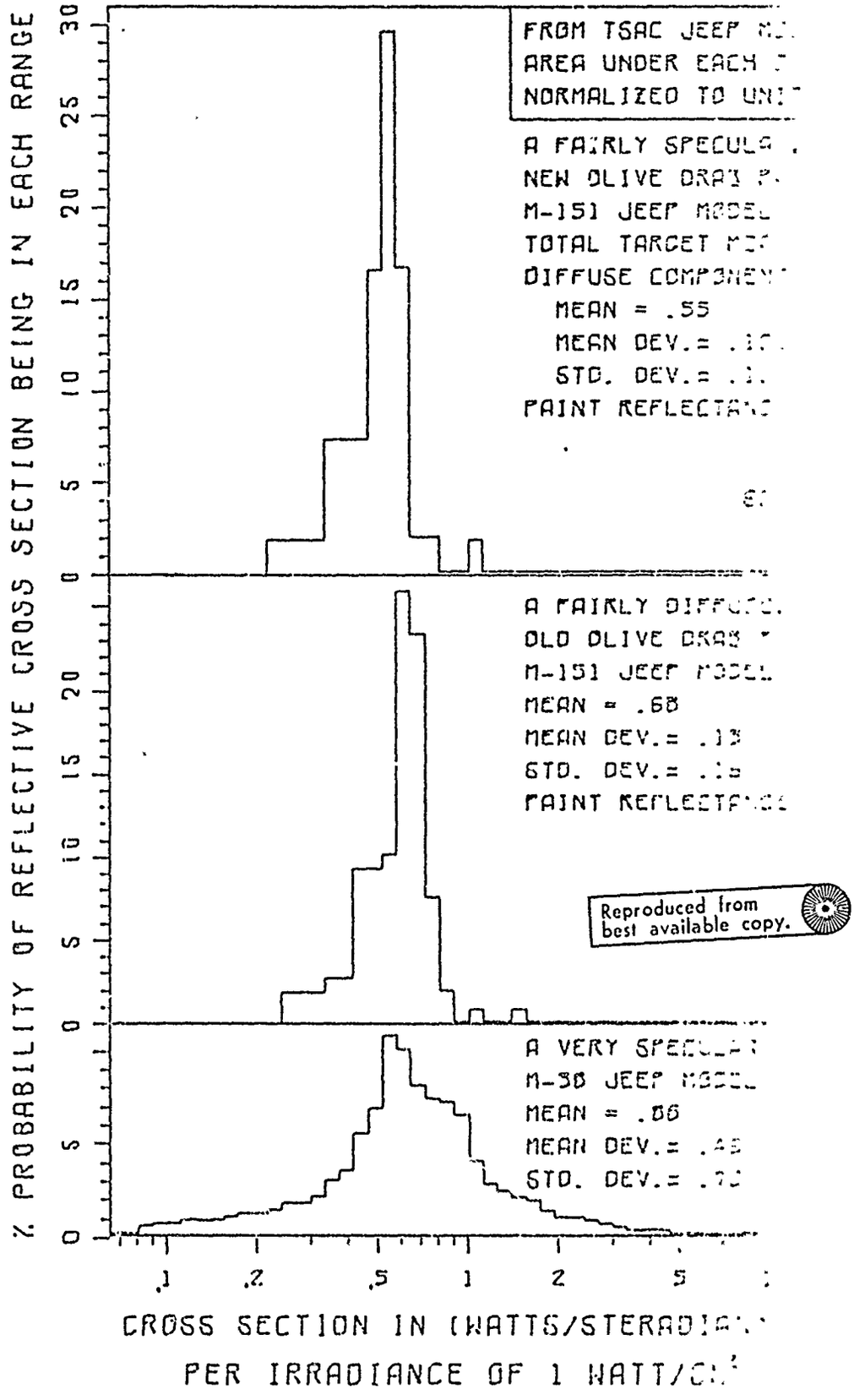

Fig. 6. Statistical Variation in Reflective Cross Section Random Angular Orientation

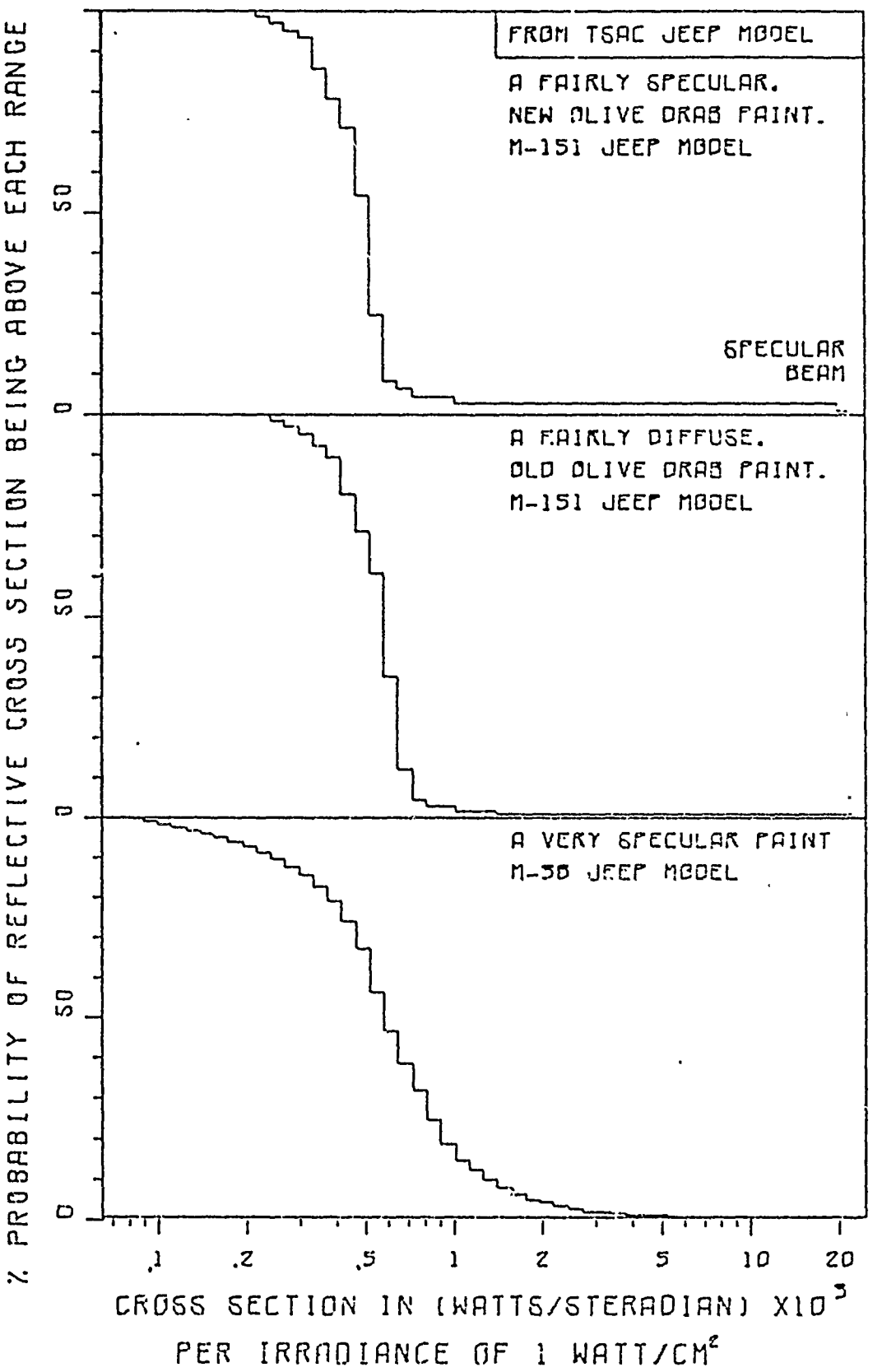

Fig. 7. Statistical Probability of Jeep Having Reflective Cross Section Above the Indicated Value

from the flat vehicle top is conspicuous. Samples taken from the jeep used in the validation tests had reflectances at 1.065 μ for new paint of 2.9 - 3.3%, old paint of 4.8 - 6.7%, black canvas of 9.3%, and olive drab canvas of 12.1% (Ref 35). Most natural vegetation and dirts have a higher reflectance range: 10 - 60%.

Computed values of σ_t were measured from TSAC charts (Ref 2, Ref 34) and the statistical probability of getting a certain reflective cross section for completely random angular orientation was computed and plotted in Figure 6. The receiver was unpolarized; the transmitter was either horizontally or vertically polarized. The probability of the σ_t being above any value was computed and plotted in Figure 7. The bottom graph of Figures 6 and 7 is of a very specular paint, not likely to be encountered in tactical combat environments, but is presented for comparison to the military olive drab, low reflectance paint, on the same jeep model. These computations are for generally clean surfaces (not mud-caked, oily, or dusty). A dusty surface has generally a much more diffuse character and a much higher reflectance (10 - 60%). Wet surfaces are completely unpredictable. This procedure for the analysis of reflective statistics of potential threat vehicles yields the maximum, minimum, and distribution of σ_t for targets under clean conditions. It is strongly recommended that these statistics be computed for many enemy vehicles of potential threat value, under many different field conditions, for wet and/or dirty surfaces.

Lock-on Range

Of the energy reflected by the target in a general direction towards the receiver, $J(\theta_r, \phi_r)$ watts/steradian, only the portion entering the effective receiving area will be available for

amplification, detection, and electronic analysis. The detector of effective area A_d (real area decreased for losses in receiver optics) and detector - target range R_d subtends a solid angle from the target of:

$$d\Omega = \frac{A_d \cos \theta_d}{R_d^2} \tag{18}$$

where θ_d is the angle between the detector normal and the line to the apparent target through the receiver optics. The cos θ_d is necessary because the detector may not be pointed along the line to the target before lock-on.

If the illuminating beam is larger than the target and has uniform irradiance, then for zero atmospheric attenuation the power received by the detector in watts becomes (from Eqs (5), (17), (18)):

$$P_d = J\,d\Omega = H\,\sigma_t\,d\Omega = \frac{4PA_d\,\sigma_t \cos \theta_d}{\pi R_d^2 (R\alpha + d_o)^2} \quad \text{in watts} \tag{19}$$

If P_{dm} is the minimum detector power in watts necessary for the receiver to acquire and track (lock-on) the target, then the maximum lock-on range is given by (from Eq (19) (for zero atmospheric attenuation)):

$$R_{dc} = \frac{2}{R\alpha + d_o}\sqrt{\frac{PA_d\sigma_t \cos \theta_d}{\pi P_{dm}}} \tag{20}$$

If the irradiance onto the target is not constant, then the energy distribution inside the beam has to be included in a new reflective cross section σ_t' (with units of steradian^{-1}):

$$\sigma_t' = \frac{J}{P} = \frac{1}{P}\int_S \rho_p H(\theta_i, \phi_i)\, dS \qquad (\text{steradian}^{-1}) \tag{21}$$

If the illuminating beam is not much larger than the target and can be approximated by a gaussian or constant irradiance beam, then Figure 3 or 4 will yield the portion K of the total beam energy intercepted by the target. Then $J = PK\sigma_t'$ and Eq (19) becomes:

$$P_d = \frac{PK\sigma_t' A_d \cos \theta_d}{R_d^2} \tag{22}$$

with a corresponding clear-air lock-on range of:

$$R_{dc} = \sqrt{\frac{PK\sigma_t' A_d \cos \theta_d}{P_{dm}}} \tag{23}$$

The maximum, minimum, and distribution of lock-on range can be determined by substituting the appropriate values of σ_t or σ_t' from Figures 6 and 7. This concept of a clear-air lock-on range, independent of atmospheric conditions, and fully descriptive of system geometry and its statistical variations, will be used frequently in this thesis.

It is generally most desirable that the attacking aircraft approach the target along the same line as the illuminator in three-dimensional space. The reflective cross section will be higher because the diffuse reflective lobe of the surface material will be greater, and the receiver will be viewing more illuminated surface.

Another effect is the reflectivity of the background. Grass, for example, exposes a much larger reflecting surface when viewed and illuminated from a shallow angle. The 1.065-μ bi-directional reflectance of grass varies from 50% (receiver overhead) to 80% (receiver at a 10° dive angle) when illuminated at a 27° dive angle (Ref 12:909). Roads, especially wet, have a much more specular reflection at low angles of illumination and show less backscatter than the surrounding fields. If the local background has a much higher reflectance than the target and is within an acceptable kill radius of the target, it will be better to illuminate the background material beside the target.

Seeker Receiver Characteristics (In General)

Laser seeker systems are classified by that characteristic which

most limits their usefullness to the target-acquisition problem. If a seeker is not cryogenically cooled, its detector housing or load resistor thermal noise will be the limiting factor (internal-noise-limited). If the detector has a low efficiency at the wavelength used or is followed by low-gain amplifiers, then it is sensitivity-limited. Either of these are termed seeker-limited systems.

The newest cryogenically cooled ($4^{o}K$) avalanche photodiodes and photomultiplier tubes approach the theoretically possible conversion efficiencies; but then these are background-limited by the flux from the terrain within the seeker field of view (5-500 milliradians). The radiance of the background may be several orders of magnitude less than the target, but due to the huge viewed area, may give more net flux at the detector. This can be improved by either using expensive, high-resolution imaging systems or narrowing the field of view until the statistical probability of the target not being in the field of view increases unacceptably. This constant solar illumination results primarily in a large DC component of the detector signal, which can be filtered out. The white noise component of the signal, however, requires considerable filtering and electronic analysis to detect the desired signal.

Most detector heads currently used are non-cooled, so are seeker-limited systems. The signal/noise ratio of these detectors varies considerably with the temperature of the detector and its load resistor. An aircraft from a hot tropical base for a low altitude flight to a local target will have a detector system at 100^{o}-$150^{o}F$, depending on how long the weapons have been sitting in the sun. The same system cruising for two hours at 40,000 feet will have a detector cold-soaked to $-50^{o}F$.

Unless compensated internally for this temperature change, the 200°F cooler temperature will have a beneficial effect of several orders of magnitude on the signal/noise ratio of the seeker and the sensitivity of the system, and hence on the lock-on range. Internal temperature compensation is therefore necessary for prediction studies and analysis.

Whether background-limited or seeker-limited the system can be a:

1. contrast-limited problem as in the electro-optical target seekers which use a high-resolution TV imaging system, or
2. "one brightest spot in the field of view" problem, or
3. "centroid of entire illumination in the field of view" problem.

System 1 is the most electronically complex and expensive, and has the disadvantage that the operator must designate the target with a pointing device in the same imaging system. Systems 2 and 3 have the problem that the portion of the laser energy falling into the more reflective background may create a brighter return than the desired target. The same problem is created when haze, clouds, or foliage is in the beam between the illuminator and the target. The seeker will either track the brightest of the targets available or the centroid. As a centroid seeker gets closer to the target, it will eventually reach a point where one of the bright spots reaches the edge of its field of view, and then will change course to attempt to track the remaining target or targets.

This problem can be considerably alleviated by designing arrays and logic circuits that discriminate against extended returns from clouds, haze, and flat terrain, and discriminate for first/last pulse of the proper strength and shape to be from a sudden, hard surface too large to be tree branches and too small to be a sloping hillside.

Seeker-limited systems are limited by their lack of sensitivity,

and high internal noise; and require illuminances on the order of 10^{-3} to 10^{-5} watts/cm^2. Background-limited systems can work with illuminances on the order of 10^{-8} to 10^{-10} watts/cm^2 with commercially available cryogenically cooled detectors. The latter are more expensive, require considerable field maintenance, and are not rugged for field use, but if the problems with pulse-shape-analysis and multi-target discrimination can be solved, they can extend the useful seeker clear-air lock-on range by the square root of the increase in sensitivity. In this author's opinion, this is the present serious limiting factor in extending the lock-on ranges of laser-guided systems.

This chapter has discussed systems in general and not any one operational system specifically. The information is a general summary of the characteristics and problems of system types in general, based on over 300 unclassified reports and articles. This completes the chapter on the geometry and design of laser systems in the absence of an attenuating atmosphere. The next chapter will deal with the physical nature of that aspect of the lock-on range problem.

III. Attenuation Mechanisms & Atmospheric Structure

Attenuation Mechanisms

Laser beams in a real atmosphere are attenuated by absorption (both band & line, in both gases & aerosols in the optical path) and scattering (Rayleigh, Mie, and turbulence cells). This chapter will discuss these mechanisms and their effects on 1.065-μ laser beams in the bottom 10 Km of the atmosphere.

Attenuation by Gases. Water is the main absorbing gas at 1.065 μ in the lower atmosphere. Only in special industrial areas with a strong thermal inversion may there be enough concentration of specialized waste gases to cause significant attenuation at certain wavelengths. Rayleigh scattering at 1.065 μ is negligible (Ref 37:7-30).

From McClatchey (Ref 26:36,59,A3) and Eldridge (Ref 17:710) one cm of precipitable water vapor will have a transmission of 96% $\pm$ 1/2% at 1.065 μ. Since the attenuation coefficient B is defined by:

$$\beta = \frac{10}{R} \log_{10}\left(\frac{1}{T}\right) \tag{24}$$

where R is the path length and T is the transmission, this yields an attenuation coefficient $\beta_{H_2O} = 0.175 \pm 0.022$ dB/cm of precipitable water vapor in the optical path. The water content of a path can be obtained from the relative humidity and temperature by Figure 8 or as follows. By definition,

$$\text{Relative Humidity} = f = \frac{e}{e_s} = \frac{\text{existing water vapor pressure}}{\text{saturated water vapor pressure for that temperature.}} \tag{25}$$

From Haurwitz (Ref 21:9):

$$e_s = (4.58)\ 10^{\left(\frac{7.5\ t}{t + 273}\right)} \tag{26}$$

where t is the temperature in degrees C and e_s = saturated vapor pressure

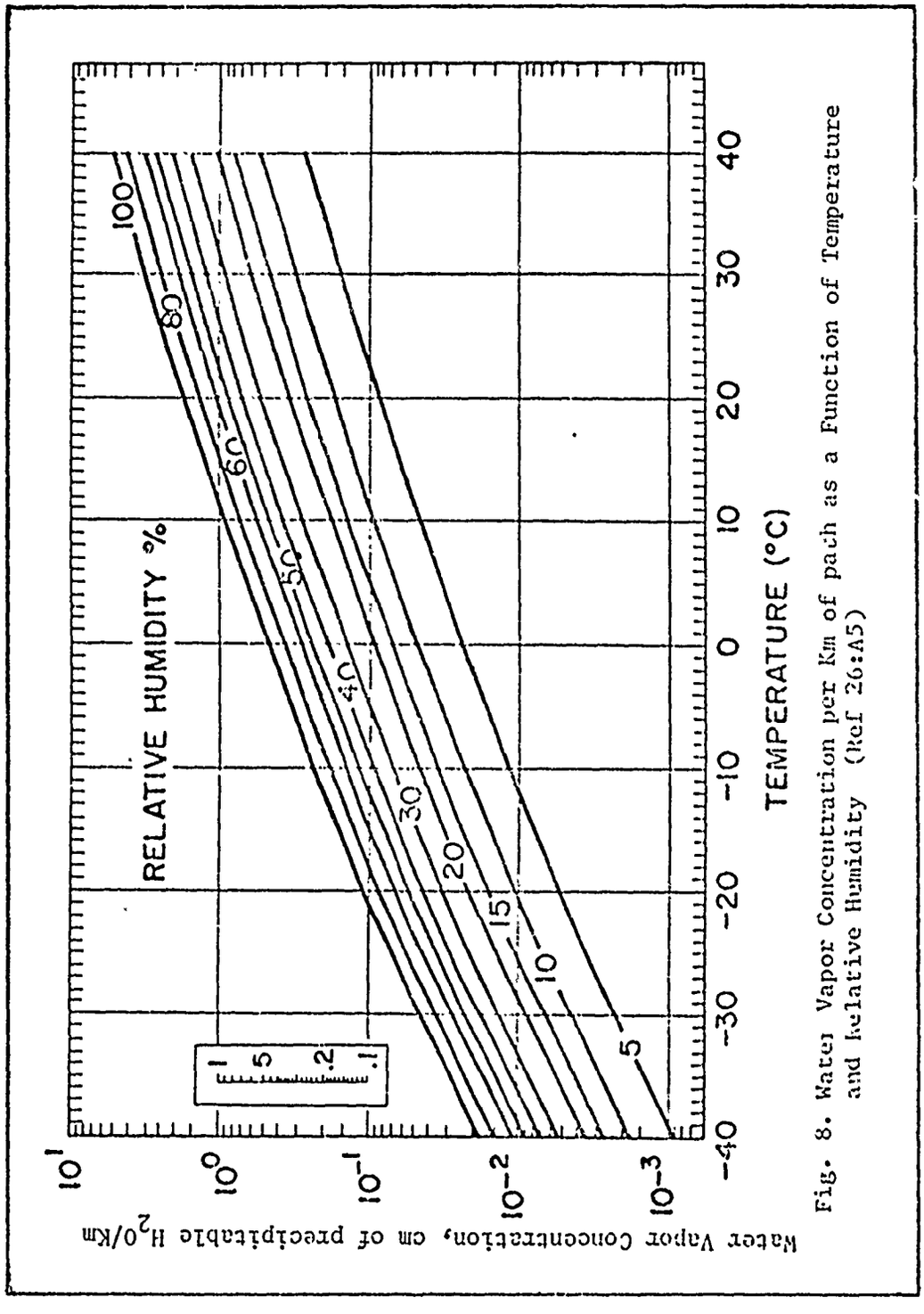

Fig. 8. Water Vapor Concentration per Km of path as a Function of Temperature and Relative Humidity (Ref 26:A5)

in mm Hg. This would match the meteorological data (Ref 26:A5)(Ref 40: 49) better if the exponent were 8.3 instead of 7.5; therefore the numeric 8.3 will be used in this thesis. From Byers (Ref 7:152,154), the absolute humidity (AH) is given by:

$$AH = \frac{em_w}{R(t + 273)} = \frac{.622\ e}{R\ (t + 273)} \tag{27}$$

where m_w is the molecular weight and R is the universal gas constant. The number of cm of precipitable water in a column of air is the absolute humidity/10 (Ref 26:A3), so combining the above information:

$$cm_{H_2O} = \frac{.622\ e}{10\ R(t + 273)} = \frac{.285\ f\ 10^{(\frac{8.3\ t}{t + 273})}}{R(t + 273)} = \frac{(136)f10^{(\frac{8.3\ t}{t + 273})}}{t + 273} \tag{28}$$

The attenuation coefficient at 1.065 μ due to water vapor is therefore:

$$\beta_{H_2O} = (.175)\ (cm_{H_2O}) \quad \text{in dB/Km} \tag{29}$$

Attenuation by Turbulence Cells. Turbulence cells (small pockets of hotter or cooler air rising or settling turbulently due to thermal convection in the atmosphere) by themselves will not absorb laser beam radiation, but they will scatter and defocus the beam locally. From one point in the beam at the target, the laser source will appear to scintillate about the average non-turbulent intensity. There will be some beamspreading, which was found by Buck (Ref 5:705) to be on the order of $d = \alpha R^{1.2}$ for l experiments at Boulder, Colorado, using an $\alpha = 4.5$ microradian beam divergence over ranges from 0.5 Km to 145 Km in relatively clear air, in mountains 2 Km above sea level. Under hazy conditions and daylight hours the exponent of R increased (Ref 5:705).

Turbulence cells will cause a statistical variation in the beam intensity, yielding a pattern analogous to Figure 2. The large target area will average these out, so the total energy reflected by the target

will not fluctuate significantly. The small seeker detector area, however, will not average the fluctuations caused by the turbulence between the seeker and the target, so there will be statistical fluctuations, up to 200 Hz (Ref 5:706) in the receiver signal. Due to the stated assumptions in pointing & tracking, beam wander is disregarded.

Attenuation by Aerosols. Absorption and scattering depend strongly on the aerosol composition and particle size distribution. The oceanic salts are the primary constituents of the soluble condensation nuclei, containing primarily the Ca, K, CO_3, Br, Cl, Sr, and Na compounds. To this is added huge amounts of insoluble materials from land soils, aromatic and organic materials from vegetation, and products of a very complex photochemical reaction of all these. The mixing ratios of these compounds vary considerably, as there is rapid transport of aerosols for at least 1000 miles (Ref 24: sect 2.3) Apparently there are no purely continental or purely maritime aerosols, but growth curves of aerosol particles with increasing relative humidity indicates that the condensation nuclei for central Europe average roughly 70 - 80% insoluble materials (Ref 24:169). The condensation nuclei have specialized composition around industrial regions, heavily vegetated regions, mountains, dusty areas, and windy areas. It takes several days for sufficient mixing to smooth out the composition mixing ratios.

Attenuation by solid, dry aerosols is a mixture of absorption and scattering. CRL aerosol analysis data (Ref 26:9,21) computes the attenuation coefficient for 1.065 μ at 23% absorption and 77% scattering for visibilities above 5 Km and relative humidities below 70%. Attenuation by wet aerosols (aqueous solutions or a thick layer of water

around an insoluble solid core) is almost entirely scattering. Above 70% relative humidity the wet aerosol particles rapidly dominate. During decreasing humidities the supersaturated aqueous solutions remain liquid down to about 40% relative humidity.

The index of refraction of water at 1.065 μ is 1.325 (Ref 10:244), and of a large proportion of materials found in aerosol particles is between 1.3 and 1.5 (Ref 13:1) with some between 1.5 and 1.7 (Ref 41: 328). Therefore the real index of refraction of aerosol particles will be between the extremes, and will be well towards the lower value for the higher humidities, where the proportion of water in the aerosol will be very large (Ref 29:6). This has been validated by attenuation measurements and calculations by Gibbons (Ref 19:172-176) within ± 4% of the theoretical values for most nonindustrial hazes.

Wet aerosols are spherical; the highly irregular shape of the dry aerosols will average out to a mean effective spherical radius since any possible orienting influence of the pulsed laser beam is randomized by the Brownian thermal motion around the aerosols. This is consistent with the dry dust scattering properties measured by Volz and Goody (Ref 38: 390). The absorption coefficient for spherical aerosol particles is approximately (Ref 29:20,22):

$$\beta_{\substack{\text{aerosol}\\ \text{absorption}}} = \pi \frac{4}{3} \int_{r_{min}}^{r_{max}} r_p^2 \left[1 + \frac{e^{-4xn'}}{2xn'} + \frac{e^{-4xn'}}{8x^2 n'^2} \right] n(r_p)\, dr_p \qquad (30)$$

where:
$n(r_p)$ = particle size distribution function.
r_p = radius of aerosol particle
n' = imaginary index of refraction of the aerosol, between 10^{-6} and 10^{-1} for most water-solution aerosols.
$x = \frac{2\pi r_p}{\lambda}$ and λ = wavelength of laser radiation = 1.065 μ.

The 4/3 in Eq (30) adjusts the approximation for a better fit of the

rigorous and exact Mie solutions. The scattering coefficient for spherical aerosol particles is given by (Ref 29:25):

$$\beta_{\substack{\text{total} \\ \text{scattering}}} = \pi \int_{r_{min}}^{r_{max}} r_p^2 \, n(r_p) \, Q_{scatt}(m, r_p, \lambda) \, dr_p \qquad (31)$$

where:

$n(r_p)$ = particle size distribution function.

$Q_{scatt}(m, r_p, \lambda)$ = Mie scattering efficiency factor.

m = real index of refraction of the aerosol.

Many-particle scattering can be neglected.(Ref 29:23) because even in the densest recorded fogs, the particles are still separated by distances over 20 times their radius. From his measurements Zuev (Ref 42: 140) determined that below 9 optical depths (1 optical depth: length at which intensity decreases to 1/e due to absorption & scattering), single scattering is valid for narrow collimated laser beams. Above 9 optical depths (=39 dB attenuation = 1/8000 origional intensity) multiple scattering may be significant for targets more than 9 times the diameter of the laser beam.

Additionally, the energy in the forward-scatter lobe broadens the beam and decreases $\beta_{\text{total scattering}}$. For small particles (haze and most clouds) the forward-scatter lobe is extremely broad, and hence the energy scattered onto the distant target is small. Snow also has a very broad lobe. Large rain particles have a strong and narrow forward-scatter lobe that decreases the total attenuation coefficient in rain by 8.4% at 0.6328 μ and 32.6% at 3.5 μ (Ref 11:735). Since the scattering raindrops were much larger than the wavelengths cited, the scattering efficiency factor Q is constant with wavelength, and therefore a linear interpolation is valid. Thus aerosol scattering is decreased by 13% at

Table II
Beamspreading as a Function of Attenuation and Type of Weather

Weather	Precip. Rate	Beam Divergence (milliradians)	Total-beam Attenuation dB/Km	Effective Attenuation at the Beam Center Caused by Broadening
Rain	clear	.209 ± .005	0	-----
	2.5 $\frac{mm}{hr}$	.295 ± .005	3.5	1.1 dB/Km
	6.5 $\frac{mm}{hr}$	.48 ± .02 (extrapolated)	5.4	2.8 dB/Km
Snow	very light	.180 ± .005	0	---
	moderate	.300 ± .005	5.0	1.7 dB/Km
	very heavy	.408 ± .005	13.65	2.7 dB/Km
Fog	clear	.182 ± .005	0	-----
	haze	.236 ± .005	3.1	0.85 dB/Km
	fog	.291 ± .005	8.5	1.6 dB/Km

(From Ref 11:753-4)

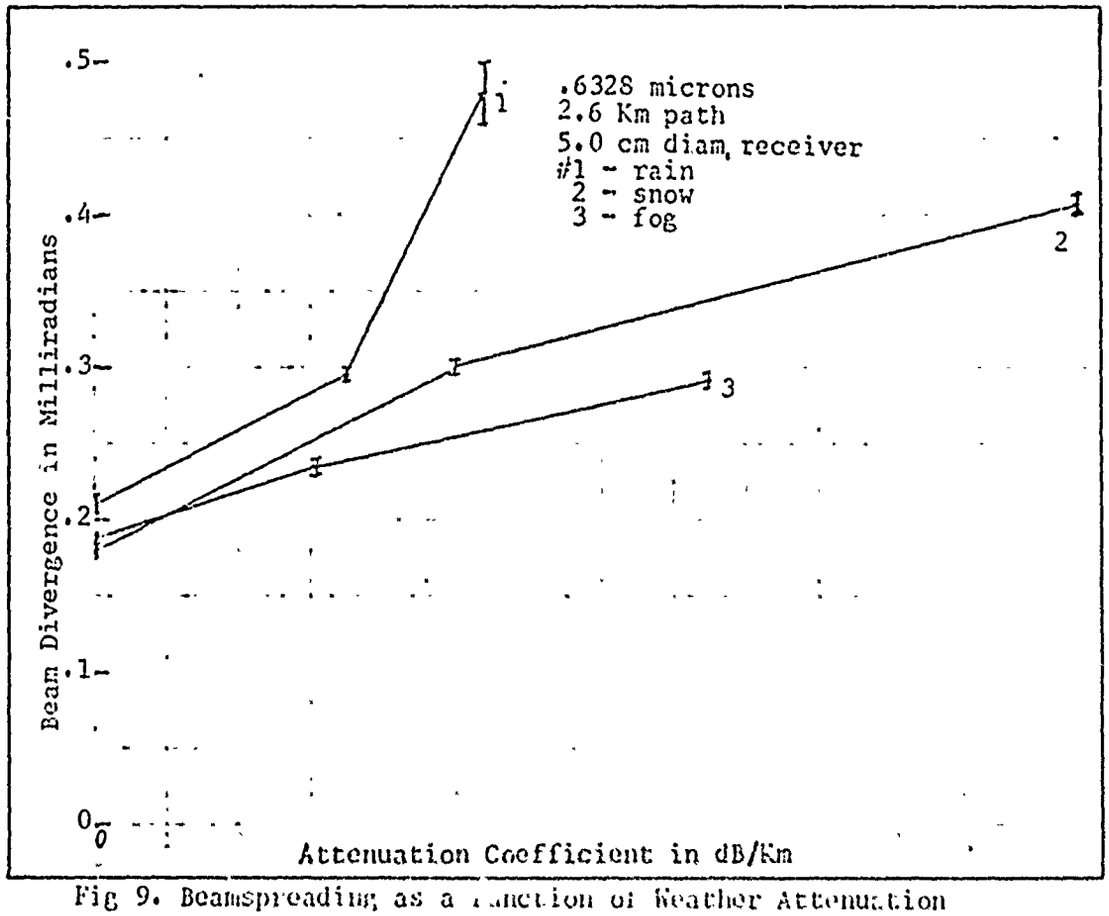

Fig 9. Beamspreading as a Function of Weather Attenuation

1.065 μ in rain.

Chu & Hogg (Ref 11:753-4) measured beam broadening of a gaussian beam over a 2.6 Km path at 0.6328 μ in rain, fog, and snow for different attenuation rates. The unattenuated beam had a whole-angle divergence of 0.2 milliradians. The results are in Table II and Figure 9. In general, the larger the beam divergence, the larger the effective forward scattering. This effect could be used effectively when illuminating large surface areas through rainstorms.

Particle Size Distributions

To solve Eqs (30) & (31) it is necessary to know the particle size distribution $n(r_p)$, and its maximum and minimum r_{max} and r_{min}. Unfortunately our knowledge in this field is very primitive. The particle size distribution has been traditionally determined by means that inherently disrupt the distribution itself or the gathering efficiency changes relative to particle size in an unknown manner.

The first method was to mount a flat, cold, dry plate and a flat, cold, oily or sticky plate (or box) outside an aircraft, facing the airflow, and fly through the haze or cloud. The collected aerosols were viewed under an optical or an electron microscope. Unfortunately the very small particles, under one micron radius and therefore exactly in the realm of interest, would follow the airflow around the plate or box, resulting in a smooth size distribution favoring the heavy particles. Secondly, the particles would evaporate in the electron microscope chamber vacuum or under the high intensity light or electron beam.

The second method was to view the aerosol particles directly through a microscope mounted at the neck of the venturi tube on the side of an aircraft. Unfortunately the considerable change in temperature,

pressure, and spacing of the aerosol particles caused rapid evaporation of the smaller liquid particles and coagulation of the larger particles.

The third method, determination of size distributions by measurements of attenuation of several laser beams through the same path, requires a prior assumption of the general form of the distribution function. A variation of this involves measuring the scattered light from the beam at different angles to determine a total scattering function for all the particles. Both yield generally acceptable approximations, but require prior assumptions about the unknown size distribution being tested. A method needs to be developed to directly study the aerosols at a distance from the aircraft that will yield a direct measurement of undisturbed aerosols.

Particles under 0.1 μ are inefficient scatterers. Particles over a 20 μ radius gradually precipitate, with settling rates proportional to mass (proportional to r_p^3) (Ref 24:111). Fog droplets range between 1 and 100 μ, while raindrops average 1000 μ. For the haze particles between 0.1 and 100 μ, the expression (Ref 29:10):

$$n(r_p) \equiv \frac{dN}{dr_p} = k\, r_p^{\delta} e^{-br_p^{\gamma}} \tag{32}$$

where:
N = number of particles with radius r_p,
k, b, δ, γ are experimentally determined constants,

is generally agreed upon as representating a final, steady-state size distribution and a first approximation to most real, atmospheric aerosols. Unfortunately the local condensation nuclei input and the dynamic atmosphere prevent a steady state condition from existing. Bimodal (double-peaked) distributions are relatively common (Ref 24:140) (Ref 17:18). It may take several days for particles under 1 μ to reach single-

mode equilibrium (Ref 24:130). Chu & Hogg modified Eq (32) by defining $a = r_p/r_m$, where r_m is the radius of the particle size with the highest number density. Eq (32) then is (Ref 11:730)

$$n(a) = k\, a^{\delta}\, e^{-ba^{\gamma}} \tag{33}$$

This representation is more flexible and in agreement with measurements from a wide range of meteorological conditions (Ref 29:12).

Below 99% relative humidity, the r_m is less than 0.1 μ, and the decrease in number density with increase in radius can be approximated by (Ref 24:116,124):

$$\frac{dN}{d(\log r_p)} \equiv \frac{r_p\, dN}{dr_p} = c r_p^{-g} \qquad \text{or} \quad \frac{dN}{dr_p} = c\, r_p^{-d} \tag{34}$$

where c, d, and g are empirical constants.

Above 99% relative humidity, the condensation process overwhelms the evaporation process for small particles, and the coagulation process dominates for the larger particles, so the r_m increases rapidly from below 0.1 μ to any value between 0.1 and 1000 μ. Rain and fog readily form. For heavy drizzle and rain, a gaussian distribution is frequently used (Ref 29:15). When a large majority of spherical particles is over 5 - 10 times the laser wavelength, a total scattering efficiency Q of about 2 can be assumed in the Mie scattering equations for wide distribution patterns, thus greatly simplifying numerical calculations. Measured and calculated particle size distributions are given in References 17, 23, 29, and others.

It must be emphasized that the real-world atmospheres are very complex, and the study of weather and particle size distributions is still in its infancy. Attenuation predictions through aerosols from meteorological measurables can be only crudely approximated.

Atmospheric Models (Vertical Structure)

The particle size distribution does not remain constant as altitude increases. The upper limit of suspended aerosol size decreases from about 20 μ at sea level to 10 μ at 3 Km altitude (Ref 24:118), with a corresponding decrease in the particle distribution between 2 μ and the upper limit for that altitude. Below 2 μ the distribution remains about the same. This settling-out is particularly noticeable for an atmosphere with no thermal mixing and no thermal inversions for several days. The heavier aerosols will settle down to an altitude where the increased density (more Brownian motion) will keep them aloft. The aerosol profile will eventually conform to the CRL exponential standard atmosphere.

If the bottom region of the troposphere up to the first strong thermal inversion has considerable convective or thermal mixing, the sedimentation process of large particles will be negated, and the result is a homogeneous atmosphere. Indeed, several cases were measured by US aircraft making whole-volume scattering measurements over Germany (Ref 18), showing a constant scattering coefficient up to the strong inversion layer, between 1 and 3 Km altitude on different days, and then a sudden decrease over the range of 200 meters in the inversion to values an order of magnitude lower than below the inversion. The measurements above the inversion showed either an exponential decreas. characteristic of a steady-state, no-mixing atmosphere, or a nearly constant and low value above that inversion layer.

Frequently in the early or mid-afternoon, the first strong inversion layer disappears due to thermal heating from below, and the formerly trapped aerosols dissipate rapidly upwards to the next

inversion layer. Equilibrium is then established within a few hours. This process may be progressively repeated through successively higher inversions. The atmosphere during the transition is somewhere between the above mentioned two extreme atmospheric states.

For calculations in this thesis, it will be assumed that:

1. The atmosphere is the same regardless of azimuth from the target, for 10 Km radius.

2. The atmosphere may be horizontally stratified, exponential and unstratified, or homogeneous. The first case will be modeled after flight test data given by Dr. Robert W. Fenn (Ref 18), from his analysis of data of Flight C139, Haven View, on 3 June 1970, near Memmingen, Germany. The second case will be modeled after AFCRL field measurements (Ref 37:7-1). The third case will be modeled after the results of the first case.

3. The atmosphere everywhere within the 10 Km radius of the target has a relative humidity below 99%: no fog or stratus layers exist with a different particle size distribution.

The first condition is very restrictive. The atmosphere in any one layer is inhomogeneous. The calculations will give an average, best, or worst case depending on the corresponding attenuation coefficient used. Multi-transmissometer studies at airfields at Atlantic City, New York City, Chicago, Denver, and Los Angeles (Ref 31) show that when visibilities are reduced to 2 Km or less, that 25% variations often occur in atmospheric transmissivities between successive readings 15 seconds apart at the same point, even when the transmissometer averages over 15 seconds observation time. Furthermore, the three transmissometers along a 3 Km runway path show incoherent fluctuations, as the

inhomogeneties form, dissipate, and drift about. When the visibility is below 0.5 Km, 600% fluctuations often occur. Above 3 Km visibility, the local variations average out because the observer can see over a longer path and the attenuation coefficients are much lower. These tests were made with light in the visual range, but the results are equally applicable to the very nearby 1.065 μ interest of this thesis.

The last condition is also very restrictive. As the aerosols rise above the inversion layer, the temperature drops rapidly and the relative humidity increases suddenly. Thus stratus layers frequently form at the top of the inversion layer, with resulting severe attenuation for those few hundred meters in the stratus layers.

Even with these three restrictions, useful and meaningful information can be obtained from the evaluation of the three cases of atmospheric models listed above. With these models of the vertical profile of the atmosphere and the models of the particle size distribution, it is now possible to combine them and determine the attenuation of a laser beam in a real atmosphere, if all the previously mentioned empirical numbers are known as a function of measurable meteorological parameters.

Attenuation Coefficients and Weather Phenomena.

At 1.065 μ:

$$\beta_{\text{total attenuation}} \equiv \beta = \beta_{H_2O} \quad \text{(From Eq (29)} + \beta_{\substack{\text{aerosol} \\ \text{absorption}}} \quad \text{(From Eq (30)} + \beta_{\substack{\text{aerosol} \\ \text{scattering}}} \quad \text{(From Eq (31)} \qquad (35)$$

Since raindrops average 1000 μ in radius, much larger than 1.065 μ, the scattering attenuation (corrected for forward scattering) is (Ref 22:6-10)

$$\beta_{\text{aerosol scattering}} = 0.88\ h^{0.683} \quad \text{dB/Km} \qquad (36)$$

where h = mm of rain per hour. Since rain is almost totally pure water, $\beta_{\text{aerosol absorption}}$ is much less than $\beta_{\text{aerosol scattering}}$.

The attenuation properties of snow (almost completely scattering) are complex, but in general the attenuation for dry powder snow is much less than that of an equivalent amount of water in the form of rain. Wet snow, however, has a thin liquid water surface over an irregular surface much larger than the laser wavelength, attenuates much more than an equivalent amount of rain, and falls more slowly (Ref 22:6-14).

The total atmospheric attenuation is the integral of Eq (35) along the entire optical path. A correlation of $n(r_p)$ with something readily measurable by weather observers is not yet known; but within certain limits of weather and wavelength some approximations can be made.

For haze with relative humidity less than 99%, the particle size distribution can be crudely classified as continental or maritime or a combination of the two, as defined by Junge and modified by Chu & Hogg. Figure 10 plots the computed total aerosol attenuation coefficients from the CRC Handbook of Lasers (Ref 40:43), CRL Optical Properties of the Atmosphere (Ref 26:15,16,19,21) and CRL Vertical Attenuation Model (Ref 33:28-47). All are representative of typical aerosols.

If aerosol scattering is the primary attenuating mechanism, perhaps a way around the lack of knowledge of precise particle size distributions is to measure the attenuation at two wavelengths relatively close (compared to the breadth of the distribution) to the 1.065 μ laser wavelength. Since both the continental and maritime hazes (and therefore a mixture of the two) cover the range from 0.02 - 10 μ (and fogs up to 100 μ) a reasonable choice for the other wavelengths would be at 0.42 μ and 0.695 μ in the visible spectrum. Measurements of attenuation at

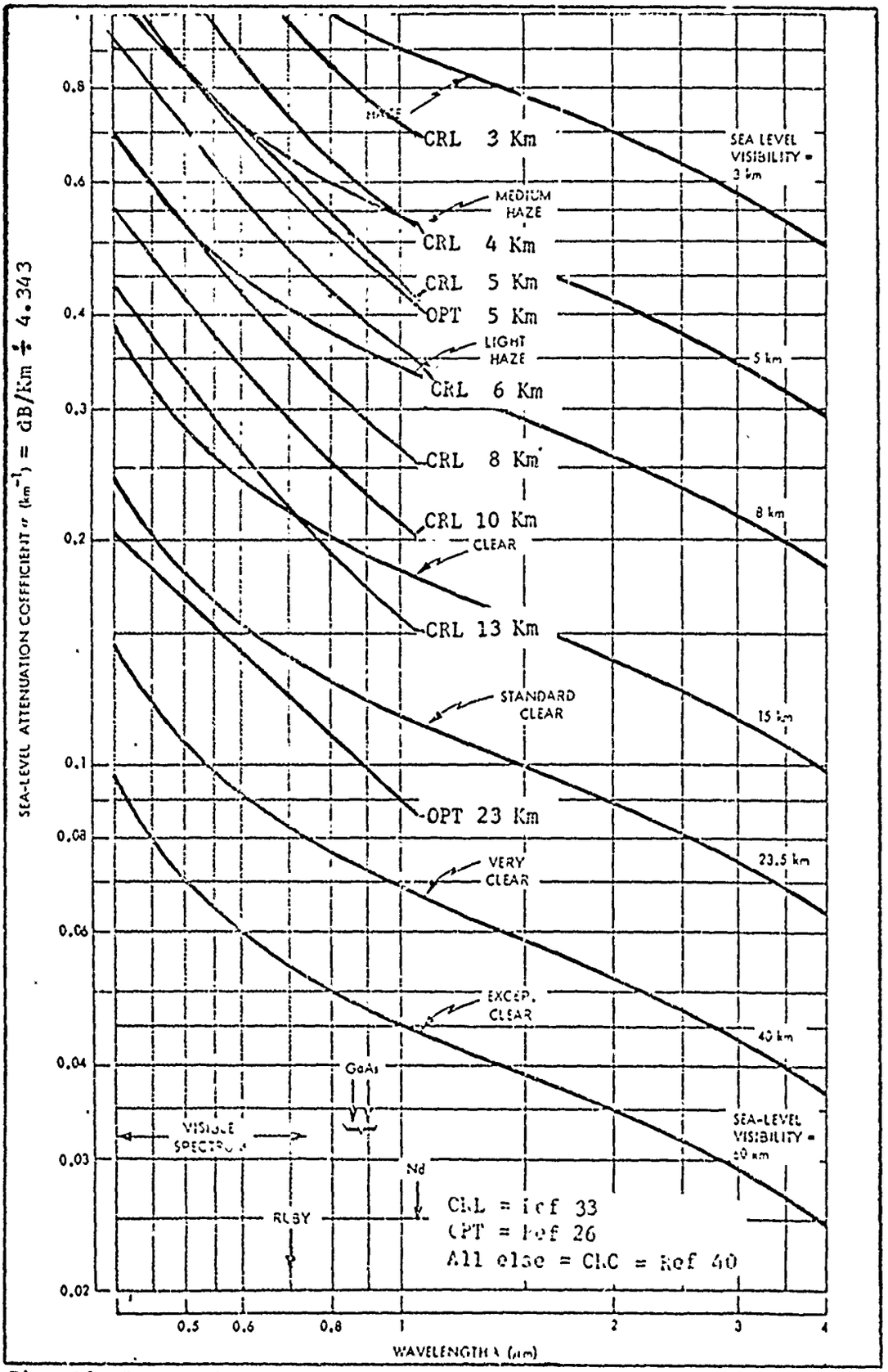

Fig. 10. Computed Aerosol Attenuation Coefficients from Three Sources (Ref 40:43) (Ref 33:28-47) (Ref 26:15-21)

these wavelengths can be measured by measuring the meteorological range through narrowband filters at these wavelengths. If the particle size distribution is broad compared to the spacing between 0.42 and 1.065 μ, does not have sharp peaks near or between these wavelengths, and is not multi-modal (or if so, it has all modes above one micron), then there should be some simple relationship between the attenuation at the three wavelengths above. This criteria are met by almost all hazes, fogs, and clouds.

Meteorological range (visibility, or meteorological visibility) in white light is the distance at which the observer can barely detect a very large, black object against a white background (apparent contrast is reduced from unity to 2%). Due to a lack of information about the contrast threshold of the photopic eye as a function of wavelength, it will be assumed that the eye can detect this 2% contrast in narrowband red light and narrowband blue light as well as in white light. This yields a relation between the attenuation coefficient β and the meteorological visibility V_{true} (from Appendix D):

$$\beta = \frac{17.0}{V_{true}} \quad \text{in dB/Km}$$

The reported visibility from weather observers is generally about 75% of the true meteorological range (Ref 18) because:

1. Perfectly black objects on a perfectly white background are ideal cases, nonexistant in field conditions.

2. There are a limited number of objects around the observer, statistically reducing the chances of one being exactly at the meteorological range. The next object inside the meteorological range will be reported if its inherent contrast is close enough to unity.

3. The observer reports the objects he can identify. The contrast

threshold for recognition is higher (about 5%) than for detection (defined at 2%). Therefore Eq (37) becomes:

$$\beta = \frac{12.8}{V_{\text{visually measured}}} \tag{38}$$

where $V_{\text{visually measured}}$ = reported visibility = apparent visibility. The reported (rather than true) visibility will be used in this thesis. If the true visibility were to be used, the spectral characteristics and inherent contrast of all visible objects around the observer for all weather conditions and sun angles must be tabulated, so when the observer reports that he can see object X, the true meteorolcgical range could be determined from the previously tabulated data. This is never done, and it is the intent of this thesis to arrive at a methodology by which an observer without considerable equipment can provide information which will allow the determination of the attenuation coefficient of 1.065 μ laser beams in real atmospheres.

The irradiance from the sun is not uniform with wavelength, but decreases by 30% at 0.42 μ and by 20% at 0.695 μ, compared to peak yellow irradiance (Ref 37:16-2). The sensitivity of the eye at 0.42 μ and 0.695 μ is less than 1% of the peak yellow-green value (Ref 20:841). This severe decrease in perceived light will make meteorological range determinations more difficult and may change the contrast threshold of the eye.

Rayleigh scattering must be subtracted from the attenuation observed at blue wavelengths and water vapor absorption added to the attenuation at 1.065 μ to make the attenuation coefficient comparison meaningful. At 0.42 μ, Rayleigh scattering is 0.16 dB/Km at sea level (Ref 16:7-5). Water vapor absorption will range from near zero to 0.9 dB/Km.

Attenuation coefficients computed by Carrier (Ref 8:1212) as a function of wavelength for clouds show a series of smooth, flat curves from 0.488 to 1.065 μ, plotted in Figure 11. The size distribution functions of lines 1, 2, and 3 have small but noticeable tails of large droplets over 6 μ; the functions for lines 4, 5, 6, and 7 have smaller and less significant tails; and line 8 has practically no tail. Note the difference that the tail of large droplets makes in the total attenuation coefficient for all wavelengths. Almost all the particles are between 1 and 15 μ in radius. Rayleigh scattering and water vapor absorption are negligible.

Attenuation coefficients were computed by Rensch (Ref 29:39,40) for a continental model aerosol with relative humidities below 90% or at 95%. The computations were made for several slopes of the distribution curve from 0.1 - 1 μ; the results are plotted in Figure 12. For relative humidities below 90% the attenuation at 1.065 μ can be determined by a linear graphical extension of the attenuation coefficients at 0.42 μ and 0.695 μ when the 0.42 μ readings are corrected for Rayleigh scattering and water vapor absorption is added for the 1.065 μ attenuation coefficient. At 95% relative humidity, a linear extrapolation of the attenuation coefficients results in an overestimation of the attenuation coefficient at 1.065 μ by approximately 0.35 dB/Km.

Similar computations by Blattner (Ref 4:29) using the Elterman haze model for meteorological ranges from 3 Km - 50 Km show that a linear extrapolation from 0.45 μ through 0.65 μ to 1.065 μ is reliable. Other calculations by Deirmendjian (Ref 14) and Cato (Ref 9) concur for relative humidities below 90% or above saturation (clouds and fogs). It is in the transition range between 90 - 100% that the aerosol particles

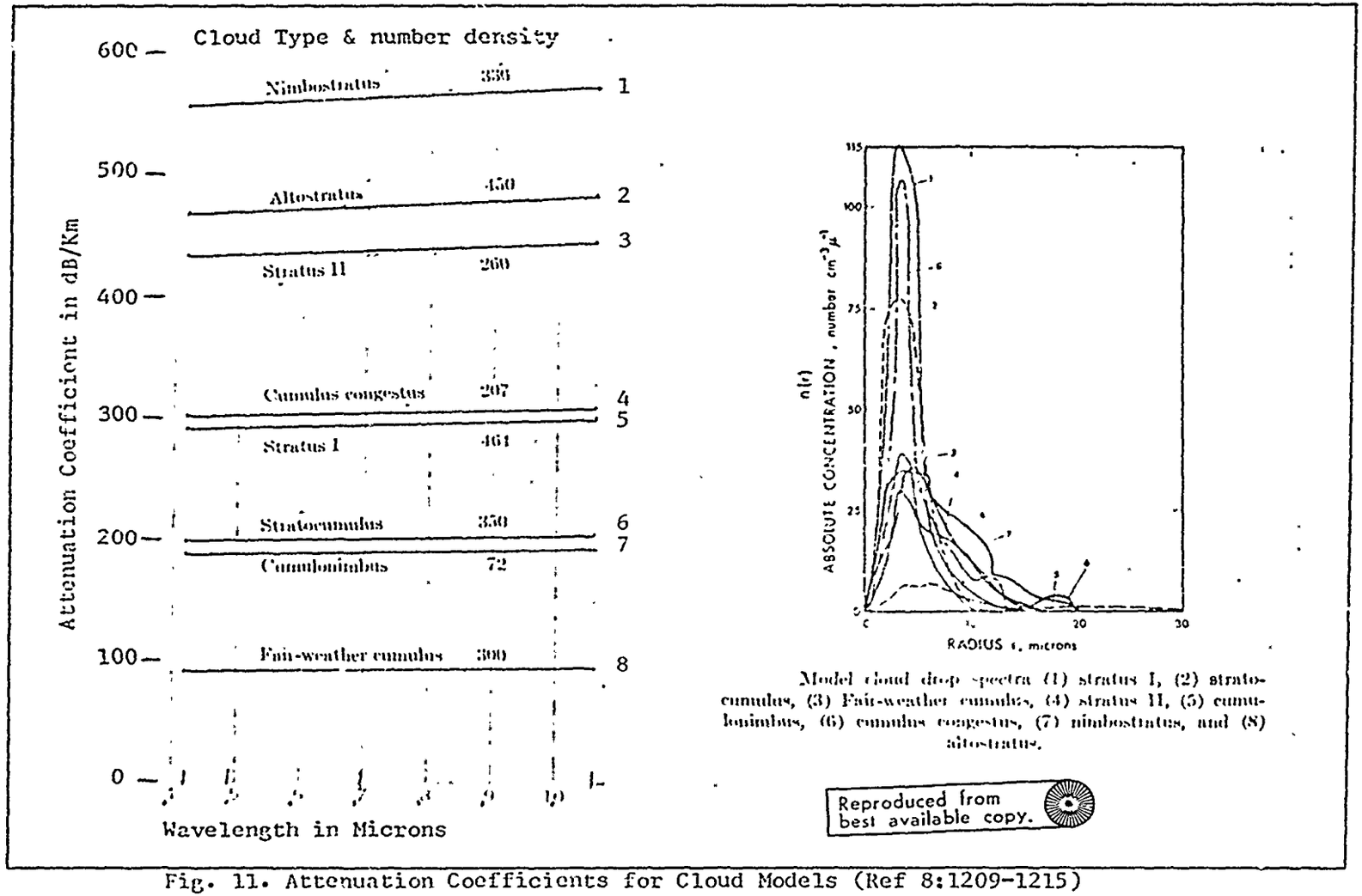

Fig. 11. Attenuation Coefficients for Cloud Models (Ref 8:1209-1215)

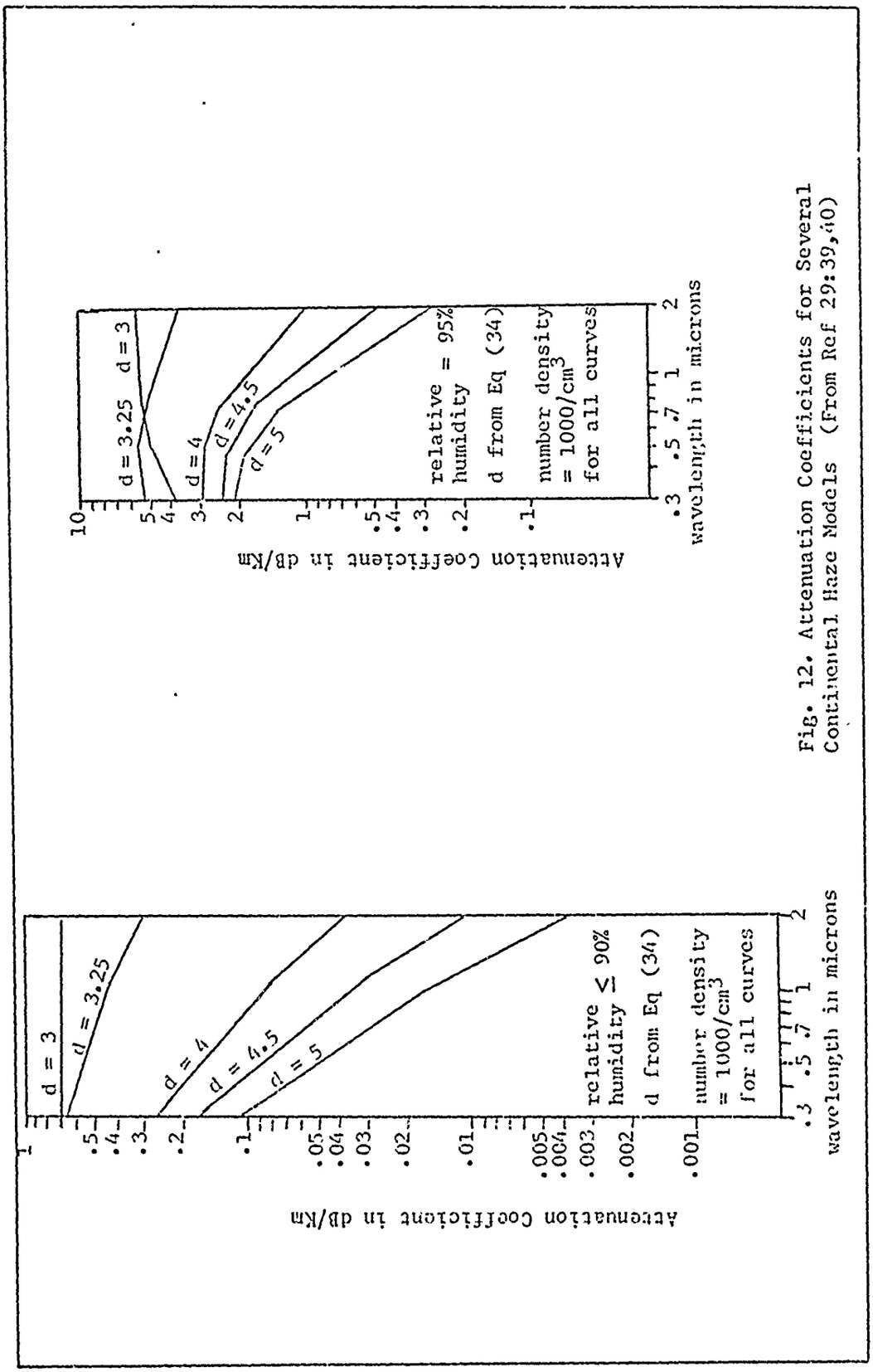

Fig. 12. Attenuation Coefficients for Several Continental Haze Models (From Ref 29:39,40)

begin to grow rapidly from below 0.1 μ into the 0.1 - 1 μ range.

There is no one-to-one relationship between relative humidity and meteorological range, but an approximate upper limit on aerosol attenuation can be deduced from measurements by Rosenburg (Ref 30:5). From his measurements of horizontal transparency and relative humidity (Figure 13) the approximate limit on minimum true visibility due to water aerosols can be determined, as in Table III.

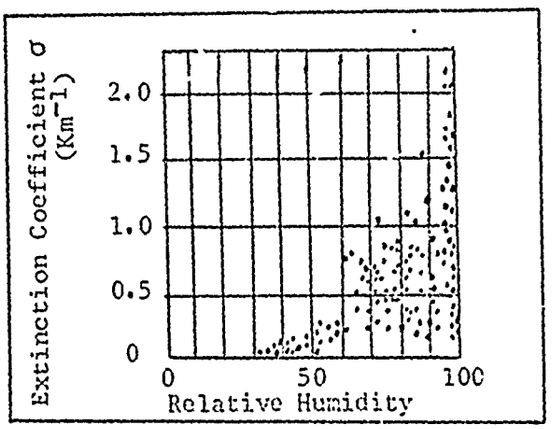

Fig. 13. Extinction Coefficient vs. Relative Humidity (Ref 30:5)

Table III
Approximate Limit on Visibility vs. Relative Humidity

% Relative Humidity	30	40	50	60	70	80	90	100
Maximum σ (Km^{-1})	.05	.15	.3	.8	.8	1.2	1.8	--
Minimum σ (Km^{-1})	.05	.05	.05	.05	.05	.05	.05	.05
Approx. minimum true visibility due to scattering (Km)	80	26	13	5	5	3.2	2.1	0

It is in the region of 80 - 100 % relative humidity that visibilities can go below 3 Km and the particle size distribution start to shift its peak from below 0.1 μ to above 2 μ for clouds and fogs. This transition depends on the ratio of soluble to insoluble condensation nuclei and the recent history of the aerosol. For cases are not within the state of

the art at this time or in the forseeable future.

Therefore a linear extrapolation of the attenuation coefficients at 0.42 μ and 0.69 μ, when corrected for Rayleigh scattering and water vapor absorption, will yield:

1. a good approximation of the attenuation coefficient at 1.065 μ, for visibilities in haze above 3 Km, with relative humidities below 90%;

2. a good approximation in fogs or clouds or haze with a visibility under 1 Km and humidities of 100%;

3. a fair approximation in the transition range between haze and fog, between relative humidities of 90-100%, and between visibilities of 1-3 Km. In this region the extrapolation will slightly overestimate the attenuation coefficient at 1.065 μ. Due to the errors inherent in measuring meteorological range, this effect is probably negligible.

This linear extrapolation method yields the attenuation coefficient at one ground position. This can be inserted into the bottom of the homogeneous, exponential, or stratified model atmosphere to get an attenuation coefficient as a function of altitude. From the illuminator-target range and target-receiver range this can be used to yield a total atmospheric attenuation. This will be accomplished in Chapter 4.

IV. Lock-on Range in a Real Atmosphere

Nominal Lock-on Ranges

In a real (attenuating) atmosphere the transmission T_i through the illuminator-target optical path R is given by:

$$T_i = 10^{-.1\int_0^R \beta(R)\, dR} \tag{39}$$

and the transmission T_d through the target-detector path R_d is given by:

$$T_d = 10^{-.1\int_0^{R_d} \beta(R_d)\, dR_d} \tag{40}$$

The clear-air lock-on range R_{dc} given in Eqs (20) and (23) are related to the true lock-on range R_{dt} by:

$$R_{dt} = R_{dc}\sqrt{T_i T_d} \tag{41}$$

The system parameter R_{dc} is independent of weather. The weather parameter T_d is independent of receiver system design because the receiver area is small. T_i is very slightly dependent on target area due to beamspreading, significant only for narrow beams illuminating large targets.

If the receiver and illuminator are together in the same aircraft, $R = R_d$, $T_i = T_d = T$, so:

$$R_{dt} = R_{dc}T \tag{42}$$

For a homogeneous atmosphere, often encountered below a strong thermal inversion, β = constant and Eq (42) becomes:

$$R_{dt} = R_{dc}10^{-.1\beta R_{dt}} \tag{43}$$

for all dive angles. The solution to this equation is plotted in Figure 14 for β from 0 to 40 dB/Km, which covers the entire range of flying

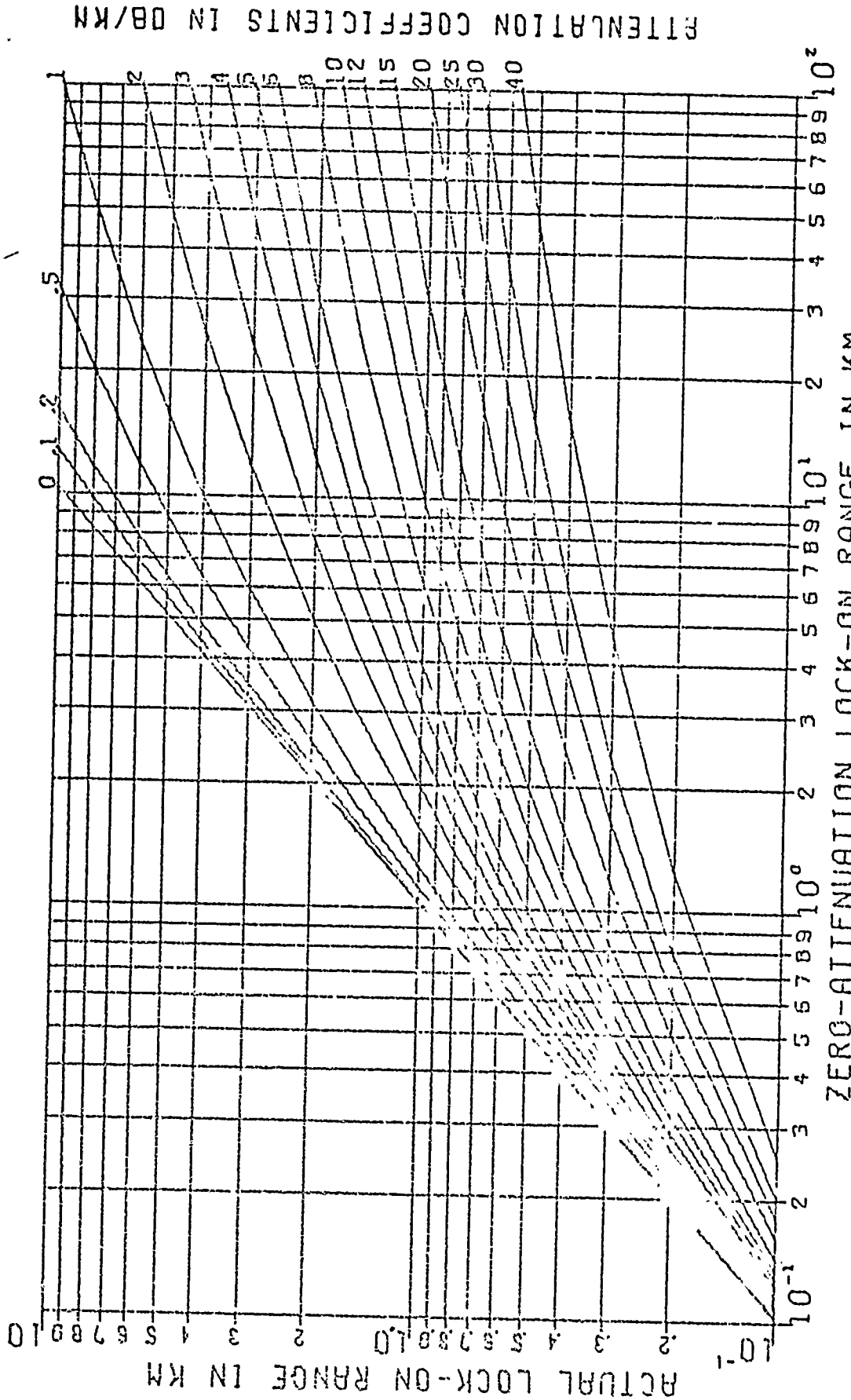

Fig. 14. Homogeneous Atmosphere, Any Dive Angle

weather conditions normally encountered. At short ranges there will be a significant but not prohibitive differences between R_{dt} and R_{dc} for most laser-guided systems for most weather conditions. At ranges beyond 3 Km, weather conditions can easily be encountered that do not prohibit flying by visual references but do prohibit a reasonably priced laser-guided system from locking on to the target prior to launch.

The problem can be worked in reverse, going from a statistical climatological analysis through attenuation coefficients and their statistical variation, through this chart to a desired clear-air lock-on range from which a system can be designed. It was stated once before in the development of the zero-attenuation case, that increasing the receiver sensitivity would increase the zero-attenuation lock-on range by the square root of the increase. This is true for the "clear air" case, but for the attenuating atmosphere case the actual increase will be somewhat less. A knowledge of the climatological statistics is necessary to predict the exact amount. If, for example, from Figure 14 the expected atmospheric attenuation is 5 dB/Km (about 2 mile visibility) and a system is designed for a zero-attenuation lock-on range of 2 Km, then it will have an actual lock-on range of 0.8 Km. If the receiver sensitivity were increased by 100 times (very easy to do for present operating systems) then the zero-attenuation lock-on range would be increased to 20 Km. Following the same 5 dB/Km attenuation line up to a new zero-attenuation lock-on range of 20 Km, however, yields an actual lock-on range of 2 Km, or what the system was designed for in the absence of an atmosphere. If the visibility were to double, the actual lock-on range would increase by 65% for this combination of atmospheric attenuation, system lock-on range, and homogeneous atmosphere.

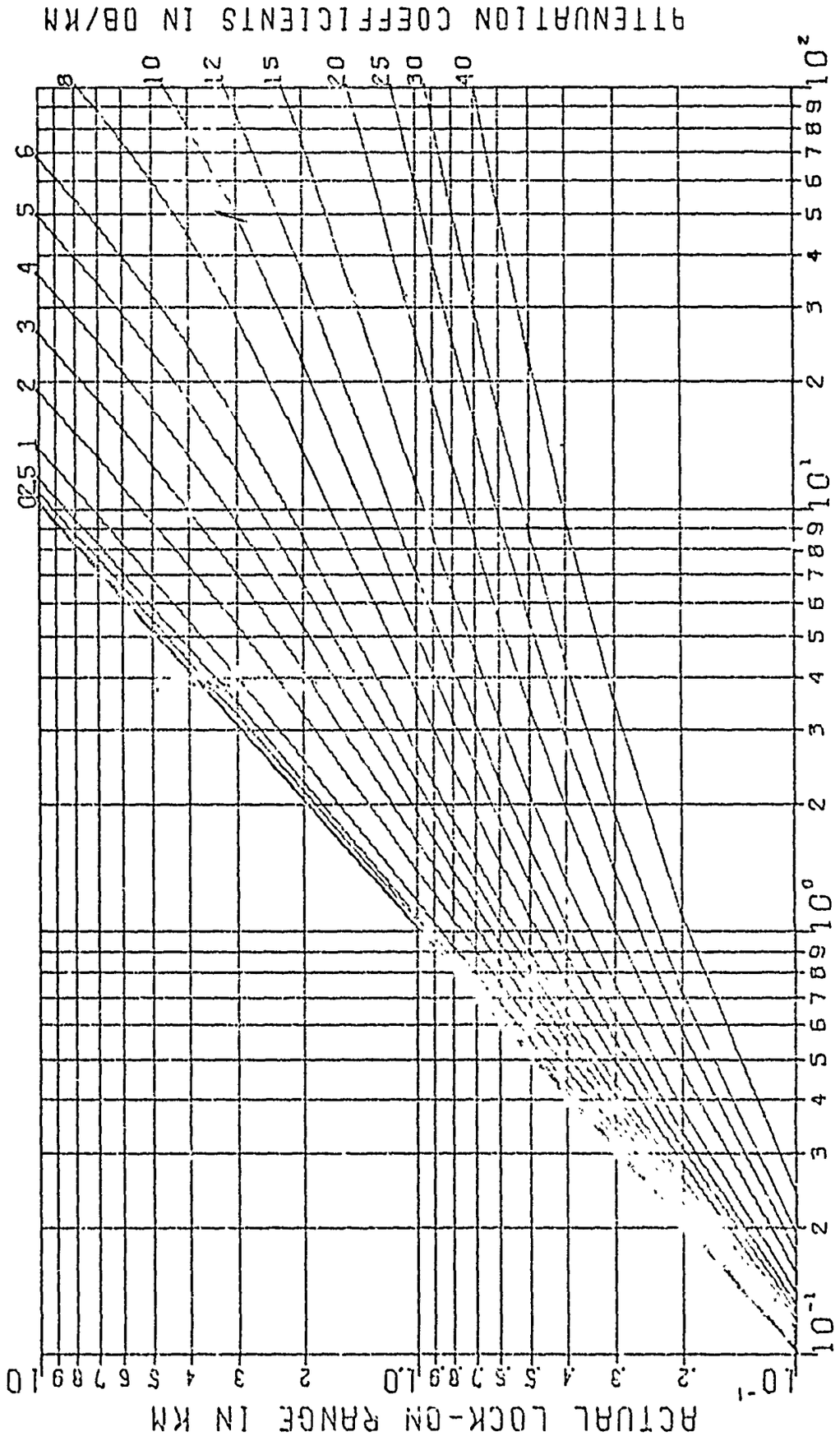

Fig. 15. Exponential, Unstratified Atmosphere, 60° Dive Angle

For an exponential, unstratified atmosphere, $\beta = \beta_{(h=0)}\exp(-h/1.2)$ (Ref 37:7-1), where the height scale factor 1.2 is an average of a large number of field measurements. Therefore if θ is the aircraft dive angle and the height $h = R \sin \theta$, then:

$$R_{dt} = R_{dc}10^{-.1\int_0^{R_{dt}}\beta(R)dR} = R_{dc}10^{-.1\,\beta(h=0)\int_0^{R_{dt}} e^{-R\frac{\sin\theta}{1.2}}dR} \qquad (44)$$

Eq (44) was solved and plotted in Figure 15 for a 60° dive angle and for $B_{(h=0)}$ from 0 to 40 dB/Km. Plots for 10°,15°,30°, and 45° dive angles are in Appendix C. AFCRL data (Ref 37:7-3) shows that this model can be used up to a 10 Km altitude.

The graph for the 10° dive angle is nearly the same as the graph for the homogeneous atmosphere case, as would normally be expected; the differences that occur are significant only at the longer ranges and middle attenuation coefficients. The graphs shift slowly as dive angle is increased to 60°, showing steadily improving performance as the dive angle increases. It is not necessary to include curvature of the earth, as some have suggested, as the aircraft is not physically at a 100 Km range. If the system is designed so that it could acquire and track the target at a 100 Km range in a zero-attenuation situation, then in a real atmosphere with the aircraft at ranges less than 10 Km the system would lock onto the target at a range of "x" Km.

The improvement of lock-on range with increased dive angle is dependent on the target reflective cross section not increasing as dive angle increases. The importance of this fact cannot be overemphasized. It would be very misleading to imply that an increased dive angle improves lock-on range, even if all atmospheric conditions are constant. The reflective cross section of the real target as a function of dive

angle must be known to work the total problem. This is closely related to the recommendation on page 19 for follow-on studies of real-target reflective cross section analysis. If the target reflective cross section were doubled, then the problem could be considered as if the receiver sensitivity were doubled, which was discussed on page 49. It is recommended that the results of the follow-on study suggested above be inserted into this sub-problem and that charts be made of the total problem for different dive angles as was done here, but including the effects of the changing real-target reflective cross section as dive angle is increased.

For a real, stratified atmosphere, the vertical profile of a test flight over Memmingen, Germany on 3 June 1970 (Ref 18) was closely modeled by:

$$\begin{aligned} \beta_3 &= .01 \text{ dB/Km above 5 Km altitude} \\ \beta_2 &= .09 \text{ dB/Km between 1.7 - 5 Km altitude} \\ \beta_1 &= \text{varied in steps for each computation but constant in each computation from ground level up to 1.7 Km.} \end{aligned} \tag{45}$$

which were approximated from the measured total-scattering functions for red (.68 μ) and blue (.48 μ) filters on the test aircraft. On this day the thermal inversion was very strong and located at an altitude of 1.7 Km. The flight was in the afternoon so there was considerable thermal convective mixing, as evidenced by the constant scattering functions below the inversion. For these computations the bottom layer attenuation coefficient was set at various values to create a family of curves for this type of atmosphere. If the aircraft is below 1.7 Km altitude, a homogeneous atmosphere results, and the attenuation is = βR, for $h = R \sin \theta < 1.7$ Km. If the aircraft is between 1.7 - 5 Km altitude, a two-layer stratified atmosphere results, and:

$$A = \int_0^{\frac{1.7}{\sin\theta}} \beta_1 \, dR + \int_{\frac{1.7}{\sin\theta}}^{R_{dt}} \beta_2 \, dR = \frac{1}{\sin\theta}(1.7\beta_1 + .09R_{dt}\sin\theta - .153) \qquad (46)$$

If the aircraft is above 5 Km altitude, a three-layer stratified atmosphere results, and:

$$A = \int_0^{\frac{1.7}{\sin\theta}} \beta_1 \, dR + \int_{\frac{1.7}{\sin\theta}}^{\frac{5}{\sin\theta}} \beta_2 \, dR + \int_{\frac{5}{\sin\theta}}^{R_{dt}} \beta_3 \, dR = \frac{1}{\sin\theta}(1.7\beta_1 + .247 + .01R_{dt}\sin\theta) \qquad (47)$$

This stratified atmosphere problem was solved and plotted for a 60° dive angle in Figure 16. The charts for 10°, 15°, 30°, 45° dive angles are in Appendix C. The second inversion at 5 Km altitude has little effect on the lock-on range, but the inversion at 1.7 Km is very conspicuous. Above the main inversion, an increase in system-designed (zero-attenuation) lock-on range has an almost equal increase in the actual lock-on range.

This form of computation is valid for any number of inversions at any altitude. The three cases can be combined: an exponential atmosphere above an inversion and a homogeneous atmosphere below. Further, if it is known that a little mixing is occuring below an inversion of unknown strength, the homogeneous atmosphere chart can be used for a worst case and the exponential atmosphere charts can be used for a best case.

Variation in Lock-on Ranges

The nominal lock-on range will vary considerably from second to second in the tactical combat situation. The reflective cross section of a TSAC jeep model with an olive drab paint has a standard deviation of $\pm$ 28%, so the lock-on range will have a standard deviation of 14% for

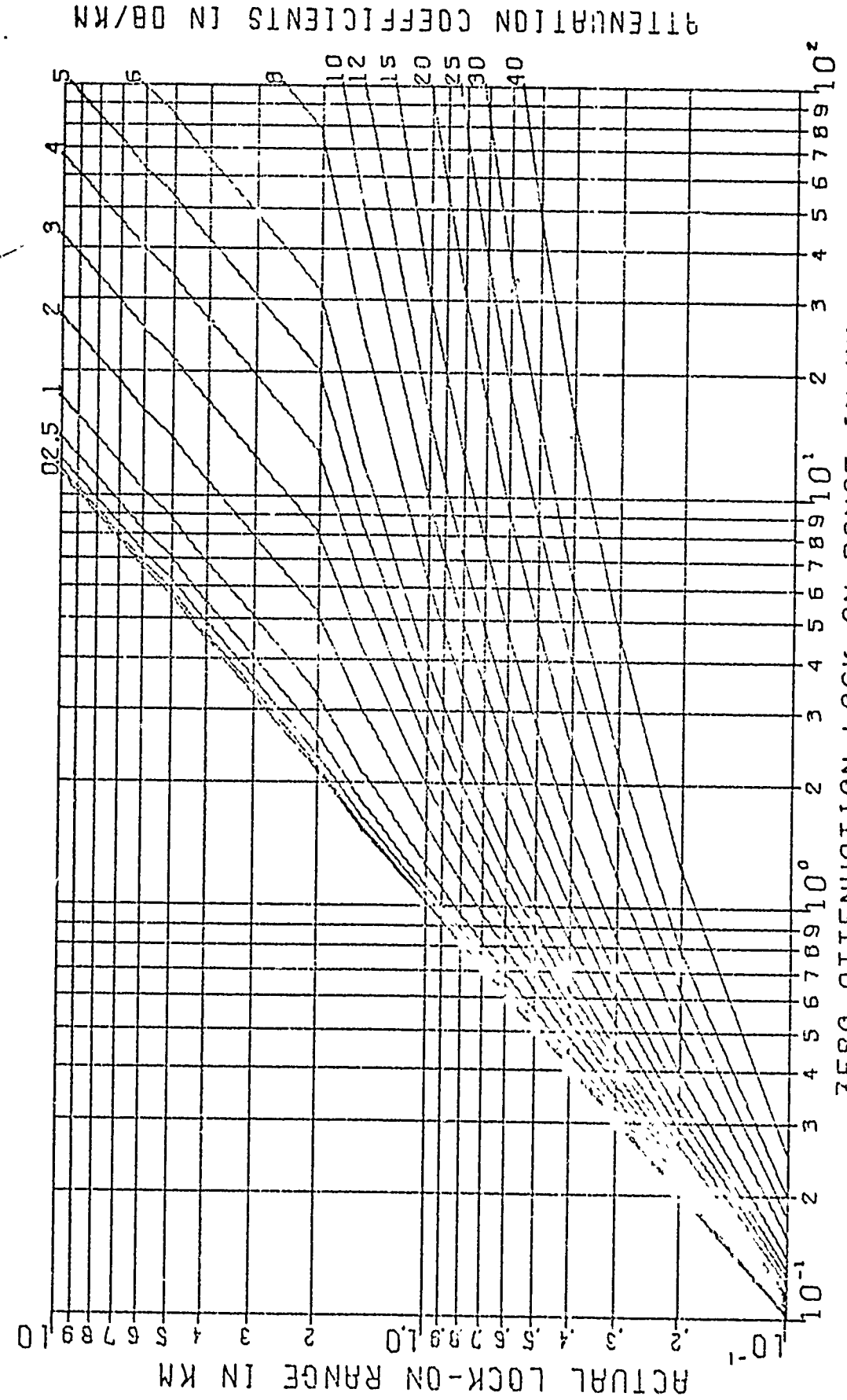

Fig 16. Stratified Atmosphere, Three Homogeneous Layers, 60° Dive Angle

that factor alone, even neglecting the bright specular reflections. In their experimental validation of their model, TSAC (Ref 2:49,53) encountered a 10% fluctuation in the power output of their military 1.065 μ laser illuminator. This author using a shoulder-fired laser illuminator encountered fluctuations of 25% many times in every 5-second firing test. A standard deviation of these laser power readings is not available, but will be approximated at ±8%. This will cause a standard deviation in lock-on range of ±4% for this effect alone.

Variations in detector threshold are extremely temperature-dependent, and unless temperature-compensated electronics are employed, will cause considerable variation in lock-on range for seeker-limited systems. Background-limited systems are not similarly affected; but they have other limitations which depend on the design of their circuit and imaging systems. The variation in cos θ_d is assumed to be small, hopefully due to proper system design. If the angle θ_d were off by an arbitrary 20°, then cos θ_d = .94, resulting in a maximum of 3% reduction in zero-attenuation lock-on range.

Atmospheric fluctuations fairly well average out when the atmospheric visibility is over 3 Km, but may fluctuate locally up to a factor of six when the atmospheric visibility is under 0.5 Km. This is an unpredictable but very significant factor when attacking a ground target surrounded by a shallow but dense ground fog or a thin stratus layer. The biggest variations in determining the attenuation coefficients are:

1. Estimating the meteorological range through optical filters. This can easily cause an under- or overestimation in the attenuation coefficient by a factor of two at the observer's position.
2. Identifying the vertical structure of the aerosol concentration of

the atmosphere, from the observer up to at least above the first strong inversion layer or stratus layer.

This uncertainty in the weather element can be greatly reduced by bouncing a lidar radar at 1.065 μ off a large tethered weather balloon as it is raised through the bottom layer of the atmosphere, and measuring the real attenuation in that atmosphere as a function of altitude. The reflectivity of the balloon could be increased to nearly 80% by spraying with aluminum paint. As the balloon is spherical, stabilization is unnecessary. Since the balloon is tethered, it can be recovered. This method should be very successful when the first strong inversion is below 1000 feet (0.3 Km), as it often is in central Europe. It was intended to experimentally test this concept but equipment and weather problems prevented actual tests. The experiments actually conducted are described in the next chapter.

V. Experimental Test of Real Atmosphere Problem

Experimental Concepts to be Tested

Goal #1 was to measure the ground-level, horizontal atmospheric attenuation at 1.065 μ, 0.695 μ, and 0.42 μ simultaneously in different haze and fog conditions, to determine if attenuation at 1.065 μ could be determined from measurements of meteorological range through narrow-band filters in the visual portion of the spectrum. Attenuation at the first wavelength was to be measured directly by firing a shoulder-mounted laser illuminator at a receiver from three known distances.

Goal #2 was to measure the slant-range atmospheric attenuation at 1.065 μ by bouncing the illuminator beam off an aluminized weather balloon and analyzing the returned signal with a telephotometer and oscilloscope. Due to the lack of funds and time, suitable receiver equipment could not be obtained during the short thesis period, so goal #2 could not be achieved.

Experimental Organization and Procedure

The shoulder-fired, Nd:YAG, repetitively q-switched laser illuminator had a diffuser cap which spread the laser beam over a 60° cone. This illuminator was fired at the receiver from distances of 70, 200, and 300 feet. The power was received by an EG&C spectroradiometer with a 100 Å monochromator centered on the laser line at $1.065 \pm 0.002\mu$. The receiver had a 14° field of view (0.18 steradian solid angle) and was electrocryogenically cooled, with an S-1 spectral response. Received signal strength was read on the large internal meter; it was not possible to modify the borrowed equipment for any other output.

Measurements were made on the roof of the AFIT School of Engineering Building 640, Wright-Patterson AFB, elevation 1004 feet above mean sea

level. Only three days between 1 Oct 1971 and 7 March 1972 had suitable weather for attenuation measurements in haze: 26 Oct 1971, 10 Jan 1972, and 20 Jan 1972. Borrowed equipment was not available on the first two days and from 24 Jan - 7 March 1972. Therefore only one day was available for measurements, although equipment and procedures were tested on several other days. On 20 January the white light visibility varied from 800 feet in dense, warm, postfrontal fog, to 7 miles in light haze below a thick overcast stratus layer. The temperature varied from 51°-54°F and the relative humidity varied from 93%-100%.

A spectral scan of the background from 1.0-1.1 μ was made at 1200 hours on a heading of 085° (magnetic) and at an uplook angle of 5° to clear the horizon, into a moderate fog fusing into a very dark, thick, low overcast.

Five complete sets of measurements were made. In each set:

1. The meteorological ranges in white light, through narrowband red, narrowband blue, and wideband red filters were measured directly by the author. The distance to the farthest visible objects was determined from base engineering maps and local aeronautical charts. Several distant buildings, telephone poles, tree lines, or other black/white objects were used to determine observed (not the true) meteorological range. If time and budget had permitted, a set of large black and white panels would have been set up in a line and photographed during the experiment through the red and blue filters for a later microdensitometer analysis of contrast degradation. The intent of the experiment was, however, to determine whether estimates of the visibility through red and blue filters could give an approximate attenuation coefficient, by quick and simple field meteorological measurements.

2. The laser illuminator with the diffusor cap on was fired at the receiver from distances of 70, 200, and 300 feet; the received signal strength was recorded. Background strength was recorded before and after each laser firing. Unfortunately there was a 25% random fluctuation in the laser signal (This had not occurred during prior trial tests.), and the meter needle would fluctuate randomly within a 25% range many times per second. It was necessary to "eyeball average" over a 5-second interval. Either the laser was not firing every time, or the pulses were not uniform in power and total energy. The meter maximum, minimum, average, and uncertainty of the average were recorded.
3. A detailed description of the weather, temperature, and relative humidity were recorded. These were compared with the Wright-Patterson official weather observations taken 5 Km northeast, and with the vertical temperature profiles taken 17 Km Northwest at Dayton Municipal Airport.

The receiver was scanned $\pm 5^{\circ}$ across the transmitter with no change in readings. The transmitter was scanned $\pm 5^{\circ}$ across the receiver with no change in readings. Therefore aiming of the transmitter or receiver was not a problem.

Analysis of Data

The spectral scan of the background sky is presented in Figure 17, which appears to be a combination of the severely attenuated solar influx which decreases with wavelength in this region, and the black-body radiation of the overcast cloud layers which increases with wavelength in this region.

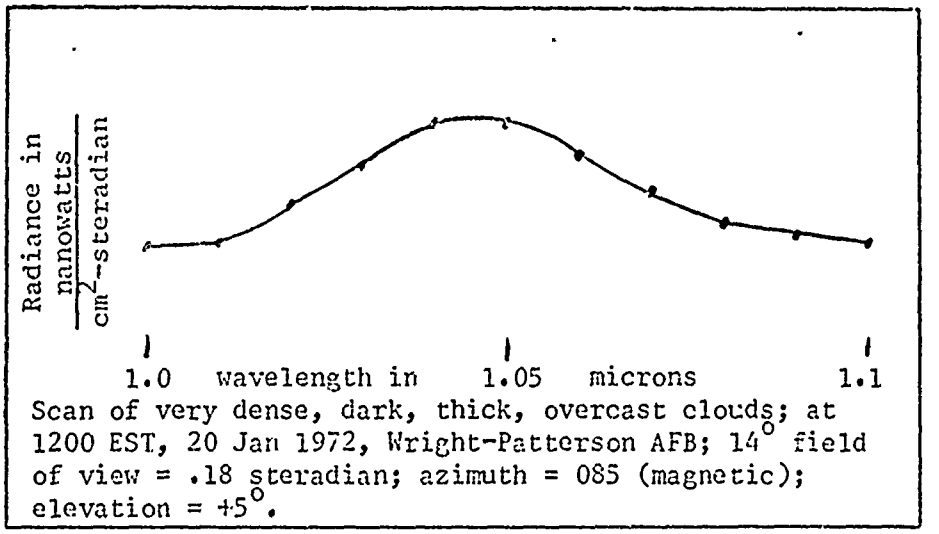

Scan of very dense, dark, thick, overcast clouds; at 1200 EST, 20 Jan 1972, Wright-Patterson AFB; 14° field of view = .18 steradian; azimuth = 085 (magnetic); elevation = +5°.

Fig. 17. Spectral Scan of the Background Sky

The experimental data is tabulated in Table IV. The attenuation coefficients are determined from Eq (38), for the wavelengths in the optical region. The laser beam attenuation coefficients can be determined by (from Appendix D):

$$\beta = \frac{10}{(R_1 - R_2)} \log_{10}\left[\left[\frac{I_1}{I_2}\right]\left[\frac{R_1}{R_2}\right]^2\right] \qquad \text{in dB/units of R} \tag{48}$$

where:

I_1 = intensity (irradiance) at range R_1

I_2 = intensity (irradiance) at range R_2

If the errors in R_1, R_2, I_1, I_2 are small, then the error in β is (from Appendix D):

$$\Delta\beta = \frac{\partial\beta}{\partial I_1}\Delta I_1 - \frac{\partial\beta}{\partial I_2}\Delta I_2 \qquad \frac{4.343}{(R_2 - R_1)}\left(\frac{\Delta I_1}{I_1} + \frac{\Delta I_2}{I_2}\right) \tag{49}$$

For large errors in any of the variables or in β, it is best to compute a new β. The results of these computations are presented in Table IV and Figure 18.

The problem of nonuniform firing within the laser illuminator was most unfortunate. The experiment was not repeated because the laser

Table IV
Summary of Data From Test
Thursday, 20 January 1972

Time (EST)	1110-1120	1145-1154	1215-1225	1310-1322	1405-1430
Filter used:	Observed meteorological range				
no filter; white light	800 feet	1600 feet	1-1/4 mile	3 miles	7 miles
wideband red	800 feet	1500 feet	1-1/4 mile	3 miles	10 miles
narrowband red	700 feet	1350 feet	5000 feet	3 miles	9 miles
narrowband blue	600 feet	950 feet	3000 feet	1 mile	1-1/2 mile
transmitter range	1.065 μ received signal strength corrected for background in amps x 10^{-10} (uncertainty of the average in parenthesis)				
70 feet	50 ±(2)	63.5 ±(3)	77 ±(4)	77 ±(6)	76 ±(3.6)
200 feet	1.5 ±(.2)	3.5 ±(.2)	8 ±(.4)	8 ±(.8)	9 ±(.4)
300 feet	zero	0.5 ±(.08)	3.3 ±(.2)	3.7 ±(.6)	4 ±(.4)
Taking each 70-foot point as base reference, the 200 and 300-foot readings for zero attenuation should be:					
200 feet	6.1	7.7	9.4	9.4	9.3
300 feet	2.7	3.4	4.1	4.1	4.1
Taking each 70-foot point as base reference, the attenuation coefficients are:					
to the 200-foot point	154 ± 10	86.5 ± 7.5	17.4 ± 7.3	17.4 ± 12.7	3.3 ± 6.6
to the 300-foot point	-------	119 ± 14.7	14.3 ± 8.0	7.1 ± 17.1	1.5 ± 10.5
mean (in db/Km)	154 ± 10	103 ± 11.2	15.8 ± 7.6	12.3 ± 14.9	2.4 ± 8.5

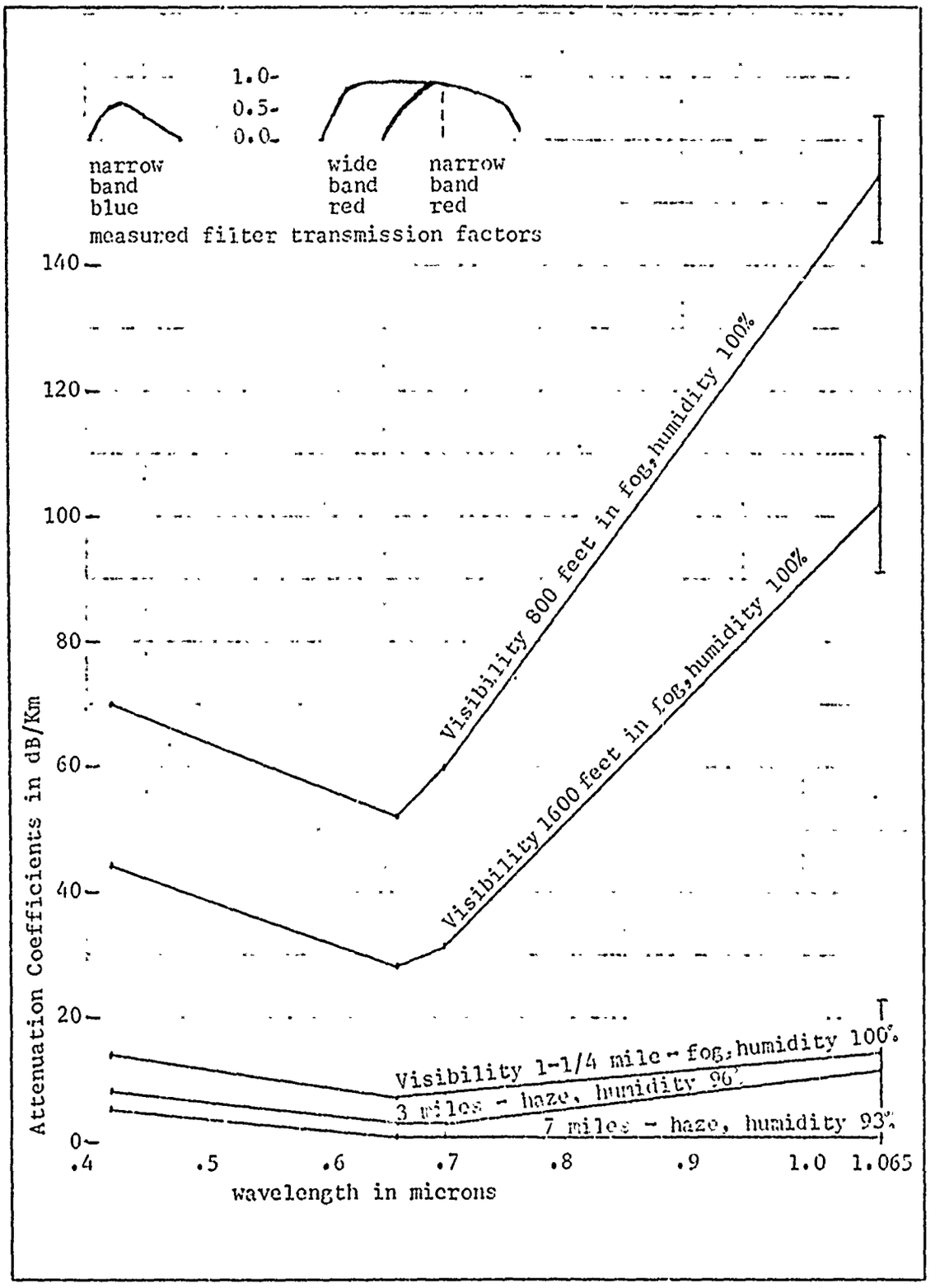

Fig. 18. Attenuation at Four Wavelengths

was not available and the weather was not sufficiently hazy. Since only the relative intensities for the three distances is used in calculations, and if it can be assumed that the problem with the laser illuminator was constant for all the firings (as it seemed to be) then the average of the meter fluctuations is meaningful.

The vertical temperature profile of the atmosphere, taken at 0700 and 1900 EST, 20 Jan 1972, and 0700 EST, 21 Jan 1972, from Dayton Municipal Airport, appears in Figure 19. A warm front passed Dayton about 1000 EST on 20 Jan 1972.

The spectral response of the three filters used in this experiment was measured on a spectral transmissometer, pointwise corrected for the zero and 100% lines, and reconstructed in Figure 20. The narrowband blue filter greatly reduced the apparent brightness of the surrounding landscape and made visibility judgement difficult. The spectral response of the blue and violet landscape also made visibility judgement difficult. The narrowband red filter likewise had the same problem as the blue and was too far towards the infrared. The wideband red filter had excellent characteristics; determination of meteorological range was far more precise and much easier. Measurement of visibility through wideband red (0.60-0.70 μ) and wideband blue (0.40-0.50 μ) filters will probably yield much more accurate results than the narrowband filters selected for this experiment. Adverse effects of the spectral characteristics of the surrounding visual references should also be reduced with the wideband filters.

Results of Test

Due to weather and equipment problems the results of this test are inconclusive. The meteorological range through the blue filter was too

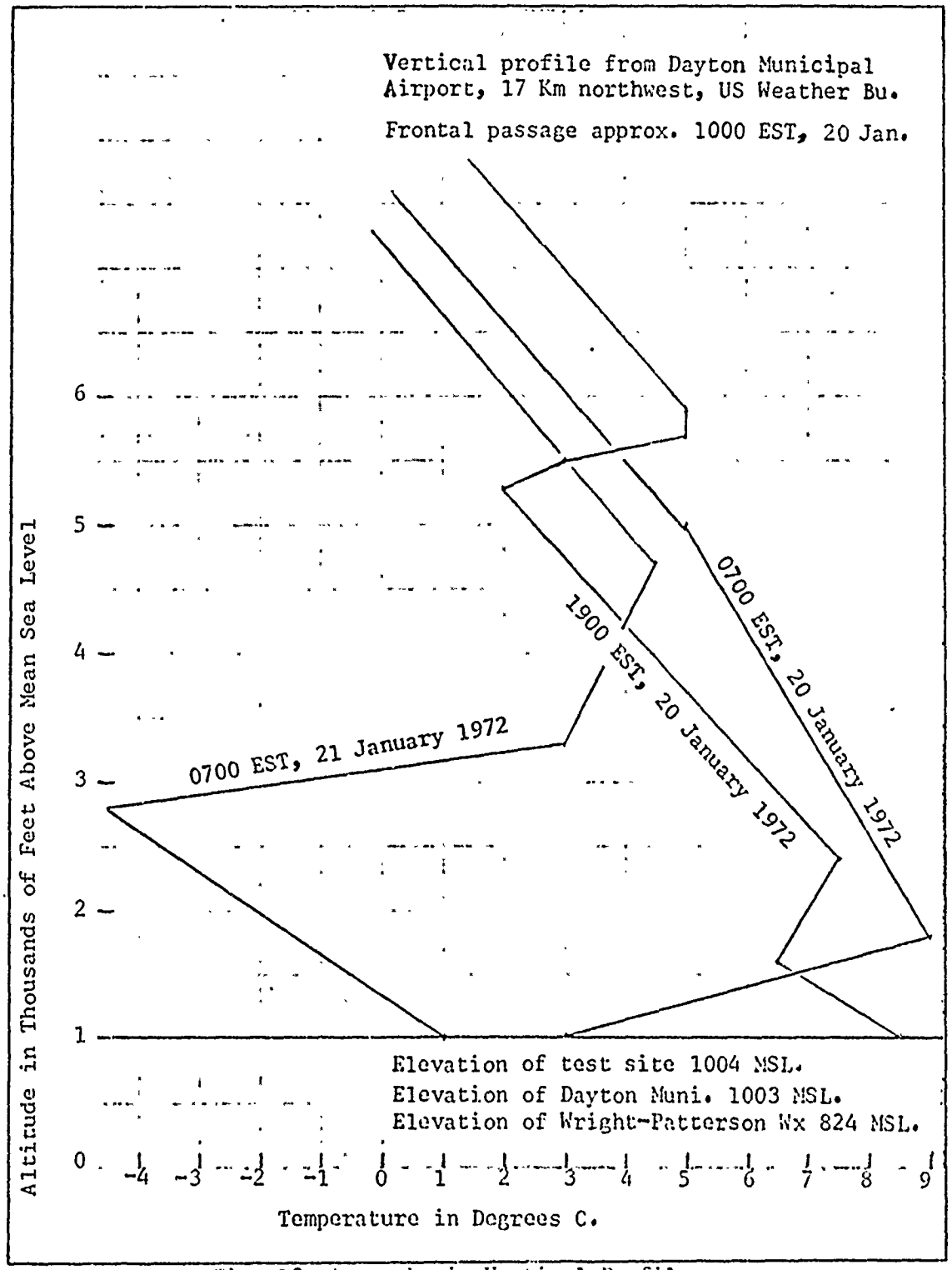

Fig. 19. Atmospheric Vertical Profile

low to match the theory. The spectral response and inherent contra. through red and blue filters of the visual references around the test site were not measured due to a lack of time. Additionally, it was desired to develop a system applicable to general field use by untrai personnel and with an absolute minumum of equipment.

This test needs to be repeated with a stable, single-mode, 1.0.7 laser illuminator, and wideband red and blue optical filters. A CW 1 is recommended.

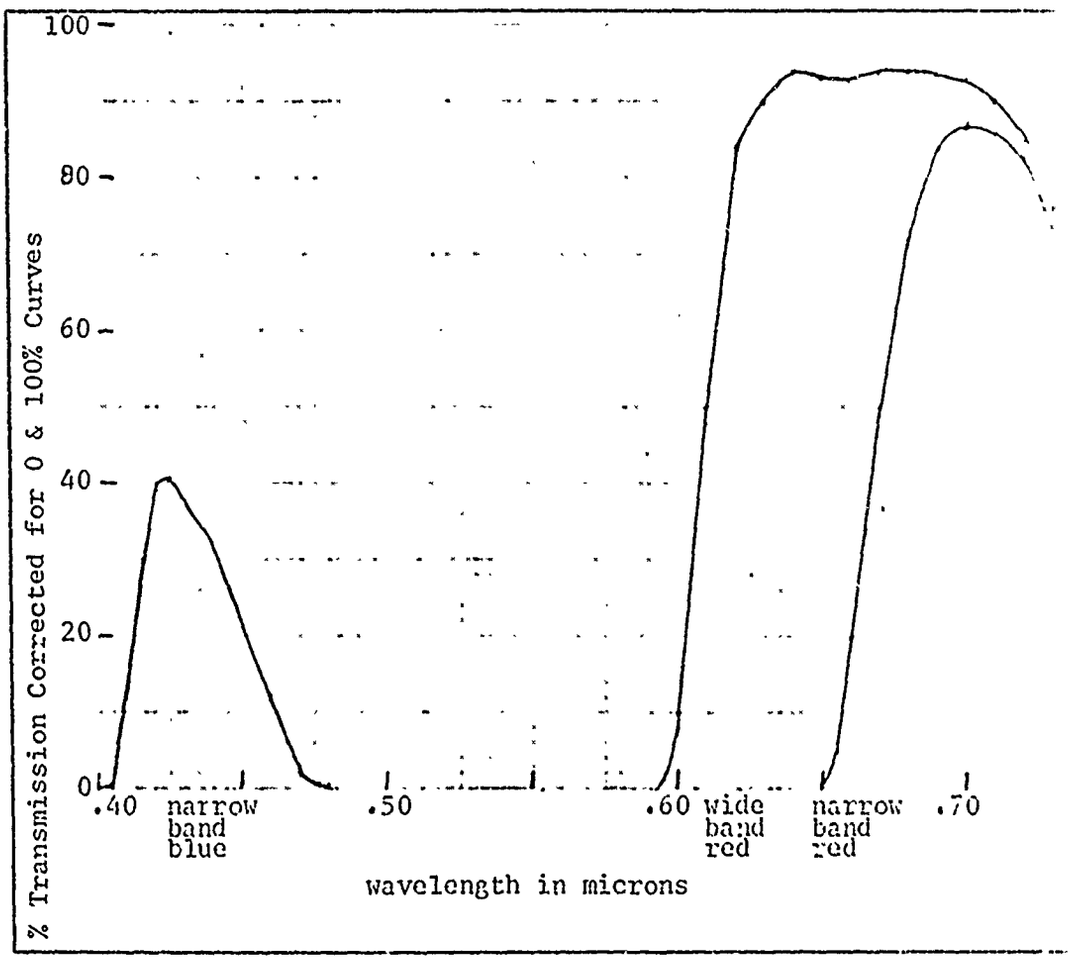

Fig. 20. Pointwise Reconstructed Spectral Scan of Filters Used

VI. Conclusions and Recommendations

1. The most serious reduction of the lock-on range at 1.065 μ is caused by the aerosol attenuation of haze, fogs, and clouds. The most important elements of aerosol attenuation are the aerosol composition and size distribution, which vary extremely with time, location, and altitude. Determination of aerosol attenuation coefficients from routine nonvisual meteorological measurements is beyond the state of the art. Relative humidity is not a useful indicator of aerosol composition or attenuation. It should be possible to determine attenuation coefficients from an extrapolation of the coefficients at nearby wavelengths in the visual range, which could be determined from measuring the visibility through wideband red and blue filters. This concept was tested against calculations and measurements of other researchers with successful results for most cases. Experimental tests of this concept were inconclusive due to equipment problems and a lack of suitable weather. It is recommended that the experiment be repeated with wideband filters and a stable, CW, laser illuminator.

2. Lock-on ranges are strongly affected by changes in the target reflective cross section, which may change by a factor of 2 - 3 times for different illumination and observation angles. The reflective cross sections of dirty or wet surfaces are unpredictable at present. It is recommended that the reflective cross sections be computed for several enemy threat vehicles for all viewing angles, for clean, wet, and dirty surfaces. It is recommended that the reflective cross section as a function of dive angle be determined, and this function be inserted in the total atmosphere lock-on range problem of Chapter IV.

3. The vertical structure of a real atmosphere can be bracketed between

an exponential, unstratified atmosphere (for no thermal mixing or convective activity for several days) and a homogeneous atmosphere (considerable convective activity below a strong thermal inversion). Computer solutions for both cases, and for a measured atmosphere from flight test data, were computed for five dive angles between 10^{o}- 60^{o} and for surface-measured attenuation coefficients between 0 - 40 dB/Km. Inhomogeneities in the atmosphere average out when the visibility is over 3 Km, but can cause fluctuations of 25% below 2 Km visibility and fluctuations of 600% below 0.5 Km visibility.

4. The lock-on range can be increased several orders of magnitude by using cryogenically cooled optical arrays and electronic circuits that discriminate against extended area returns and false targets from the highly reflective background or foreground objects also illuminated by the laser beam.

5. The contrast threshold characteristics of the photopic eye as a function of wavelength are not known. It is recommended that a black/white (black velvet/white magnesium oxide) target be viewed through many narrowband and wideband filters to determine the contrast threshold characteristics of the photopic eye as a function of wavelength and filter bandwidth.

Bibliography

1. Bailey, H.H. and L.G. Mundie. The Effects of Atmospheric Scattering and Absorption on the Performance of Optical Sensors. RM-5938-PR. Santa Monica, California: Rand Corporation, March 1969.

2. Beard, J.L. Multifaceted Target Model Validation, Fourth Informal Technical Report. 032210-33-T. Ann Arbor, Michigan: The Target Signatures Analysis Center, University of Michigan, November 1971.

3. Bell, Ely E., et al. "Spectral Radiance of Sky and Terrain at Wavelengths Between 1 and 20 Microns. II. Sky Measurements." Journal of the Optical Society of America, 50:1313-1320 (December 1960).

4. Blattner, W.G. Calculations of Atmospheric Attenuation Parameters and Angular Scattering Data for Light Scattering in Model Atmospheres. RRA-T702. Fort Worth, Texas: Radiation Research Associates, 1 March 1970. AD868745.

5. Buck, A.L. "Effects of the Atmosphere on Laser Beam Propagation." Applied Optics, 6:703-708 (April 1967).

6. Burch, Darrell E., et al. "Absorption of Infrared Radiation by CO_2 and H_2O. II. Absorption by CO_2 between 8000 and 10 000 cm^{-1} (1-1.25 microns)." Journal of the Optical Society of America, 58:335-341 (March 1968).

7. Byers, Horace Robert. General Meteorology. New York: McGraw-Hill Book Company, Inc., 1944.

8. Carrier, L.W., et al. "The Backscattering and Extinction of Visible and Infrared Radiation by Selected Major Cloud Models." Applied Optics, 6:1209-1215 (July 1967).

9. Cato, G.A., et al. Laser Systems Study. Part III. Effect of Clouds. EOS Report 4440-Final III. Pasadena, California: Electro-Optical Systems, Inc,14 December 1965. AD479487.

10. Centeno, Melchor, V. "The Refractive Index of Liquid Water in the Near Infra-Red Spectrum." Journal of the Optical Society of America, 31: 244-247 (March 1941).

11. Chu, T.S. and D.C. Hogg. "Effects of Precipitation on Propagation at 0.63, 3.5, and 10.6 Microns." Bell System Technical Journal, 48:723-759 (May-June 1968).

12. Coulson, Kinsell L. "Effects of Reflection Properties on Natural Surfaces in Aerial Reconnaissance." Applied Optics, 5:905-917 (June 1966).

13. Curcio, J.A., et al. Atmospheric Scattering in the Visible and Infrared. Washington D.C.: U.S. Naval Research Laboratory, 24 January 1961.

14. Deirmendjian, D. "Scattering and Polarization Properties of Water

Vapor Clouds and Hazes in the Visible and Infrared." Applied Optics, 3: 187-196 (February 1964).

15. Eldridge, Ralph G. "Water Vapor Absorption of Visible and Near Infrared Radiation." Applied Optics, 6:709-713 (April 1967).

16. Electro-Optics Handbook. SCN 102-67. Burlington, Massachusetts: RCA, Defense Electronic Products, Aerospace Systems Division, 1968.

17. Electro-Optical Systems, Inc. Study of Atmospheric Degradation of Laser Beams. EOS Report 7097-Final. Cambridge, Massachusetts: NASA Electronics Research Center, December 1967.

18. Fenn, Robert W. Personal communication. Optical Physics Laboratory, Air Force Cambridge Research Laboratories, Bedford, Massachusetts.

19. Gibbons, Mathew G. "Wavelength Dependence on the Scattering Coefficient for Infrared Radiation in Natural Haze." Journal of the Optical Society of America, 48:172-176 (March 1958).

20. Halliday, David and Robert Resnick. Physics for Students of Science and Engineering. New York: John Wiley & Sons, Inc, 1960.

21. Haurwitz, Bernhard. Dynamic Meteorology. New York: McGraw-Hill Book Co, 1941.

22. ITT Communication Systems, Inc. Applicability of Laser Techniques. ESD-TR-66-480. L.G. Hanscom Field, Bedford, Massachusetts: Deputy for Communication Systems, Electronic Systems Division, August 1964.AD486861.

23. Junge, Christian. "The Size Distribution and Aging of Natural Aerosols as Determined From Electrical and Optical Data." Journal of Meteorology, 12:13-25 (February 1955).

24. -----. Air Chemistry and Radioactivity. New York:Academic Press,1963.

25. Langer, R.M. Laser Beam Attenuation in the Lower Atmosphere - Part II. Arlington, Massachusetts: JRM Bege Company, 1 June 1964. AD454990.

26. McClatchey, R.A. et al. Optical Properties of the Atmosphere. AFCRL-70-0527. L.G. Hanscom Field, Bedford, Massachusetts: Air Force Cambridge Research Laboratory, 22 Sept 1970.

27. Nicodemus, Fred E. "Directional Reflectance and Emissivity on an Opaque Surface." Applied Optics, 4:767-773 (July 1965).

28. Ory, H.A. Atmospheric Effects on Laser Propagation: I. Refractive Effects. RM-5579-ARPA. Santa Monica, California: The Rand Corporation, March 1968. AD830967.

29. Rensch, David B. Extinction and Backscatter of Visible and Infrared Laser Radiation by Atmospheric Aerosol. Technical Report 2476-3. Wright-Patterson AFB,Ohio: Air Force Avionics Laboratory, 2 April 1969. AD850891.

30. Rosenburg, G.V. "The Properties of an Atmospheric Aerosol from Optical Data." Izvestiva, Atmospheric and Oceanic Physics, 3:936-949 (1967). (Translated by J. Findlay). (U.D.C. 551.593.5).

31. Schlatter, Ernest E. Evaluation of Several Multi-Transmissometer Systems. Report RD-67-72. Atlantic City, New Jersey: Weather Bureau, US Department of Commerce, December 1967. AD668990.

32. Siegman, A.E. An Introduction to Lasers and Masers. New York: McGraw Hill Book Company, 1971.

33. Elterman, Louis. Vertical-Attenuation Model With Eight Surface Meteorological Ranges 2 to 13 Kilometers. AFCRL-70-0200. Bedford, Massachusetts: L.G. Hanscom Field, March 1970. AD707488.

34. Target Signatures Analysis Center, University of Michigan. TSAC Target Reflection and Emission Model. Wright-Patterson AFB, Ohio: Air Force Avionics Laboratory, February 1971.

35. -----. Personal communication. Spectral reflectance graphs of materials provided by J.R. Maxwell.

36. V., L.M. "Rain Attenuation Model Verified." Microwaves, 11:14 (January 1972).

37. Valley, Shea L. (Editor). Handbook of Geophysics and Space Environments. New York: McGraw-Hill Book Company, Inc, 1965.

38. Volz, F.E. and R.M. Goody. "The Intensity of the Twilight and Upper Atmospheric Dust." Journal of the Atmospheric Sciences, 19:385-406 (September 1962).

39. Weather Bureau, US Department of Commerce. Aviation Weather. AC-00-6. Washington D.C.: Federal Aviation Agency, 1965.

40. Weast, Robert C. (Editor-in-Chief). Handbook of Lasers. Cleveland, Ohio: The Chemical Rubber Company, 1971.

41. Wolfe, William L. (Editor). Handbook of Military Infrared Technology. Washington D.C.: Office of Naval Research, 1965.

42. Zuev, V.E., et al. "Propagation of Laser Beams in Scattering Media." Applied Optics, 8:137-141 (January 1969).

Appendix A

Comparison of Beam Divergence Definitions

A computer program was developed to integrate the energy of a gaussian beam that was contained within a cone of increasing angular dimension centered in that beam. If K is the portion of the beam's energy within the cone, then (from Eq (2)):

$$K = \int_0^{2\pi} \int_0^{r'} \frac{c}{\pi w^2} e^{-c\left(\frac{r}{w}\right)^2} r\, dr\, d\theta = \int_0^{r'} \frac{2cr}{w^2} e^{-c\left(\frac{r}{w}\right)^2} dr = 1 - e^{-c\left(\frac{r'}{w}\right)^2} \tag{50}$$

At the 90% enclosed-energy points, K = .9000, so when $\frac{r}{w} = 1$, c = ln 10 = 2.3026. The integrating program was developed at this point to test the program against exact integral results just performed. The program integrated Eq (50) by a gauss 15-point integration subroutine GLDI from the AFIT computer center, with an interval size 1/5 of the integration limits, thus creating an effective gauss 75-point integration. The values if K were computed from $0 \leq \frac{r}{w} \leq 2.5$ in steps of 0.05 by repetitive iteration. These values agreed with the exact solution of Eq (50) to the third decimal place. The program was used soon afterwards for difficult integrals that could not be checked against the exact solutions: a gaussian beam illuminating a rectangular target.

Now to compare the relative widths of the gaussian curves. For a beam defined by Eq (2), with r as the only variable, looking at the gaussian exponential and therefore neglecting the integrating height-normalizing constant when comparing beam widths:

$$\frac{I(r)}{I(o)} = e^{-2.3026\left(\frac{r}{w}\right)^2} \quad , \text{ or } \quad \frac{w}{r} = \sqrt{2.3026 / \ln \frac{I(o)}{I(r)}} \tag{51}$$

Eq (51) gives the relationship between column 2 and column 5 in Table

I. For example, row 5: by this definition $I(r)/I(o) = 1/e^2 = 0.1353$. Therefore:

$$\frac{w}{r} = 2.3026/\sqrt{\ln (e^2)} = 1.075$$

which is the multiplicative factor for converting this defined laser beam width to the standard definition of beam width for this thesis. By setting $r = w$ and letting $I(r)/I(o)$ be as defined for each row,

$$\frac{I(r)}{I(o)} = e^{-c} \quad , \text{ or} \quad c = \ln \frac{I(o)}{I(r)} \tag{52}$$

Eq (52) gives the relation between column 2 and column 3 of Table I. For example, row 5. By this definition: $I(r)/I(o) = 1/e^2$. Therefore $c = 2.0000$. Finally, for each row, setting $r = w$, and having computed c from Eq (52), Eq (50) can be used to determine the total energy enclosed by the cone, in column 4 of Table I.

Appendix B

Integration of Beams Across Targets of Various Shapes

For a constant-irradiance cone of light falling on the center of a circular target, the ratio of power intercepted by the target (P_t) to transmitted power (P) (neglecting any atmospheric effects) is given by:

$$K \equiv \frac{P_t}{P} = \left(\frac{h}{d}\right)^2 \qquad \text{for } h \leq d$$
$$K \equiv 1. \qquad \text{for } h \geq d \tag{53}$$

where h = the vertical dimension (height) of the round target, and d = the beam diameter at the target position.

For a constant-irradiance beam of diameter d illuminating a rectangular target of height h and length nh. There are four possible cases, diagramed in Figure 21.

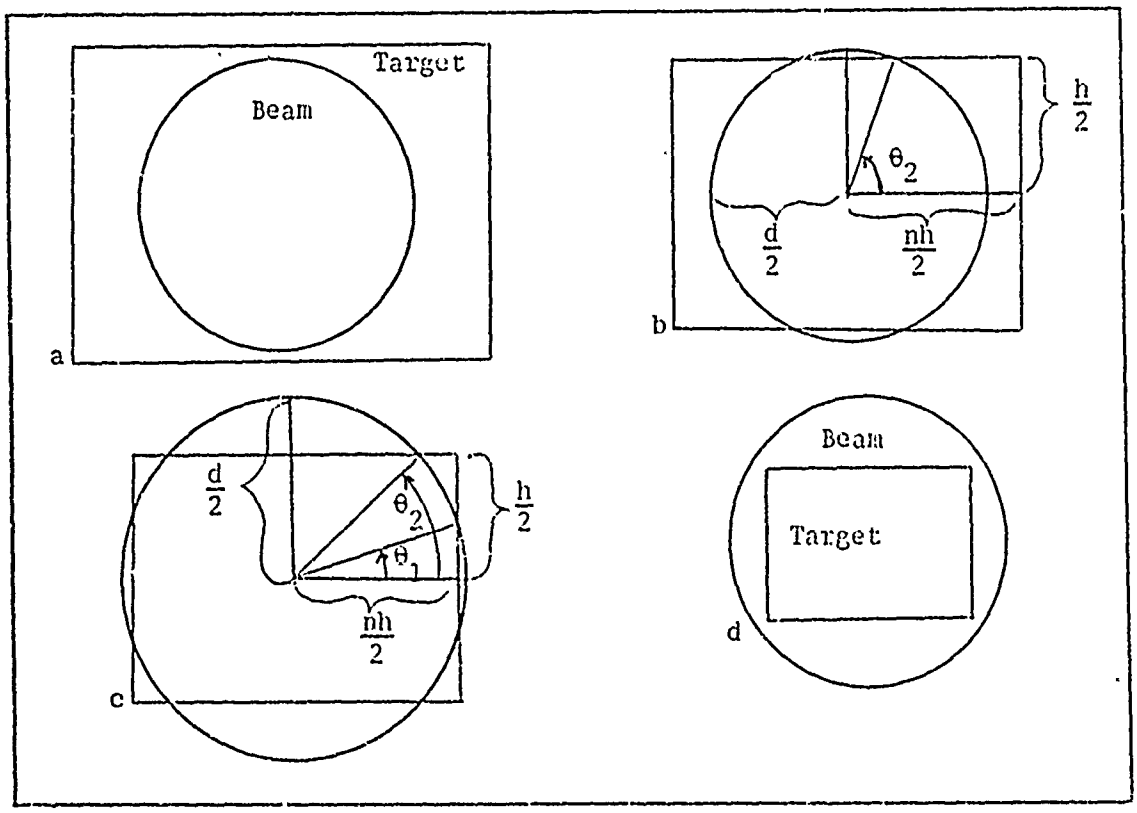

Fig. 21. Geometry of Constant Beam on Rectangular Target

Case a. When $h > d$, all the beam energy is on the target, and $K = 1$.

Case b. When $\frac{1}{n} < \frac{h}{d} < 1$, then for each quadrant, all the beam energy between $0 < \theta < \theta_2$ is intercepted plus the energy in the triangle between $\theta_2 < \theta < 90^\circ$. If the total beam energy is normalized to unity, then the irradiance is $H = 4/\pi d^2$. Since $\theta_2 = \arcsin(\frac{h}{d})$,

$$K = \int_S H \, dS = 4\int_0^{\theta_2=\arcsin(\frac{h}{d})} \int_0^{r=d/2} \frac{4}{\pi d^2} r \, dr \, d\theta + 4\int_{\theta_2=\arcsin(\frac{h}{d})}^{\pi/2} \int_0^{r=h/2 \sin\theta} \frac{4}{\pi d^2} r \, dr \, d\theta$$

$$= \frac{2}{\pi} \arcsin(\frac{h}{d}) + \frac{2h}{\pi d} \sqrt{1 - (\frac{h}{d})^2} \tag{54}$$

Case c. When $\frac{1}{\sqrt{1 + n^2}} < \frac{h}{d} < \frac{1}{n}$, then the energy intercepted in each quadrant is that in the triangle from $0 < \theta < \theta_1$, plus the circular sector from $\theta_i < \theta < \theta_2$, plus the triangle from $\theta_2 < \theta < 90^\circ$. Since $\theta_1 = \arccos(\frac{nh}{d})$,

$$K = 4\int_0^{\theta_1=\arccos(\frac{nh}{d})} \int_0^{r=nh/2 \cos\theta} \frac{4r}{\pi d^2} dr \, d\theta + 4\int_{\theta_1=\arccos(\frac{nh}{d})}^{\theta_2=\arcsin(\frac{h}{d})} \int_0^{r=d/2} \frac{4r}{\pi d^2} dr \, d\theta$$

$$+ 4\int_{\theta_2=\arcsin(\frac{h}{d})}^{\pi/2} \int_0^{r=h/\sin\theta} \frac{4r}{\pi d^2} dr \, d\theta$$

$$= \frac{2}{\pi}\left[\arcsin(\frac{h}{d}) - \arccos(\frac{nh}{d})\right] + \frac{2nh}{\pi d} \sqrt{1 - (\frac{h}{d})^2} + \frac{2h}{\pi d} \sqrt{1 - (\frac{h}{d})^2} \tag{55}$$

Case d. When all the target is in the beam, the ratio of target area (nh^2) to the beam area ($\pi d^2/4$) is the fraction of energy intercepted,

$$K = \frac{4n}{\pi}(\frac{h}{d})^2 \tag{56}$$

For a gaussian beam on targets of different shapes, the total power intercepted by the target can be solved by one case, since the gaussian

beam has no discontinuities and is very much larger than the target so can be considered filling the transmitted hemisphere. For the round target, the problem is the same as in Appendix A:

$$K = 1 - e^{-2.3026(\frac{h}{d})^2} \tag{57}$$

For the rectangular targets, no exact solution exists, so a numerical integration (from Appendix A) was used at each of 100 points from n = 0 to n = 2.5, as for the constant-irradiance problem above. Using the same nomenclature as above, with $\theta_1 = \theta_2$ at the corner of the rectangle, so θ_1 = arccot n,

$$K = 4\int_0^{\theta_1=\text{arccot}(n)} \int_0^{r=hn/\cos(\theta)} \frac{9.2104r}{\pi d^2} e^{-9.2104(\frac{r}{d})^2} dr\, d\theta + 4\int_{\theta_1=\text{arccot}(n)}^{\pi/2} \int_0^{r=h/\sin(\theta)} \text{same integrand}\; dr\, d\theta$$

$$= 1 - \int_0^{\theta_1=\text{arccot}(n)} \frac{2.3026}{\pi} e^{-\left[\frac{9.21h^2n^2}{d^2\cos^2\theta}\right]} d\theta - \int_{\theta_1=\text{arccot}(n)}^{\pi/2} \frac{2.3026}{\pi} e^{-\left[\frac{9.2104h^2}{d^2\sin^2\theta}\right]} d\theta \tag{58}$$

A computer program was created to solve and plot Eqs (54) - (58) for values of n (where appropriate) from 0 to 2.5 in steps of 0.025, for a circle, square, and rectangles.

Appendix C

Lock-on Range Charts

These eight charts are discussed on pages 51-53.

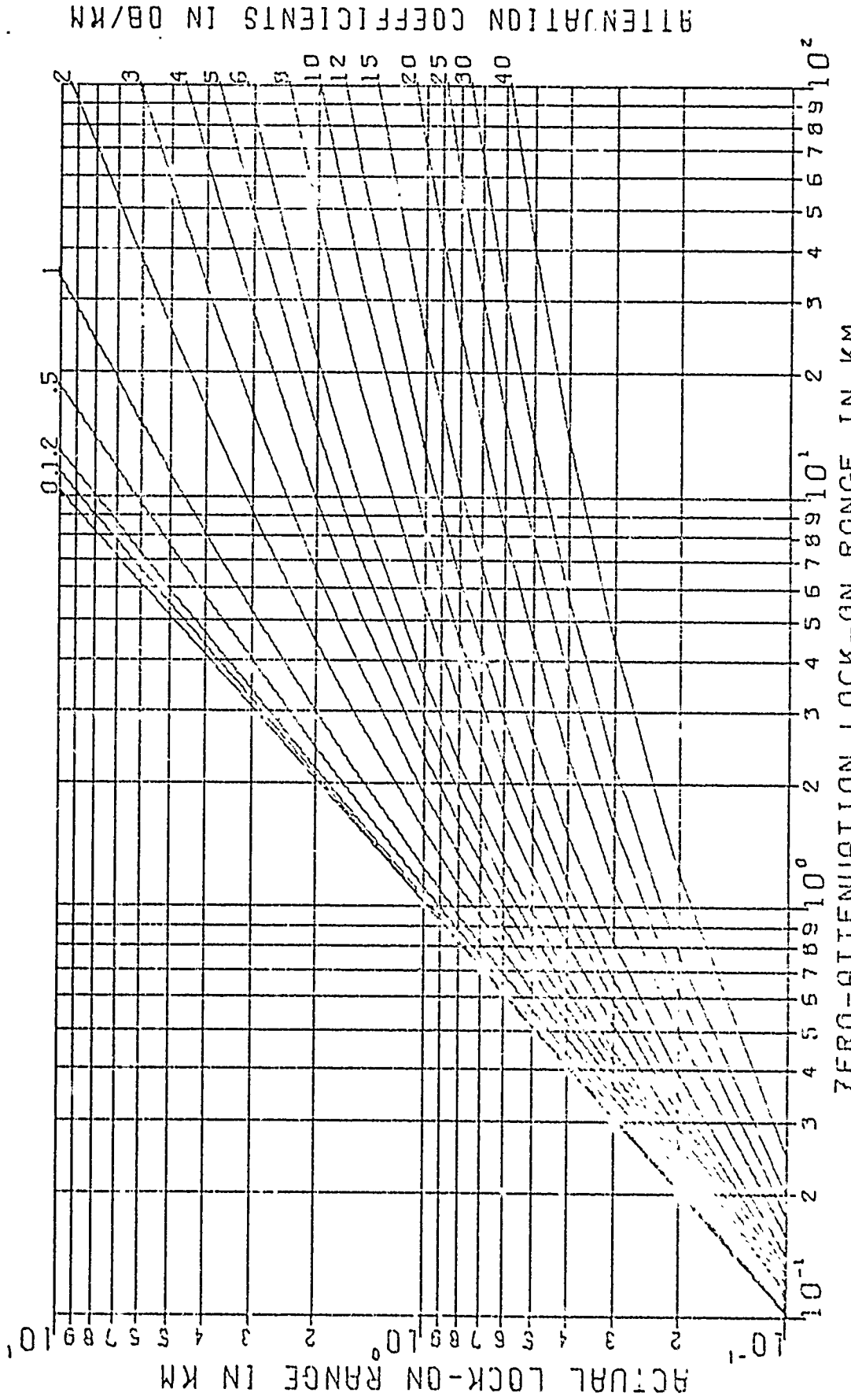

Fig. 22. Exponential, Uncratified Atmosphere, 10^{0} Dive Angle

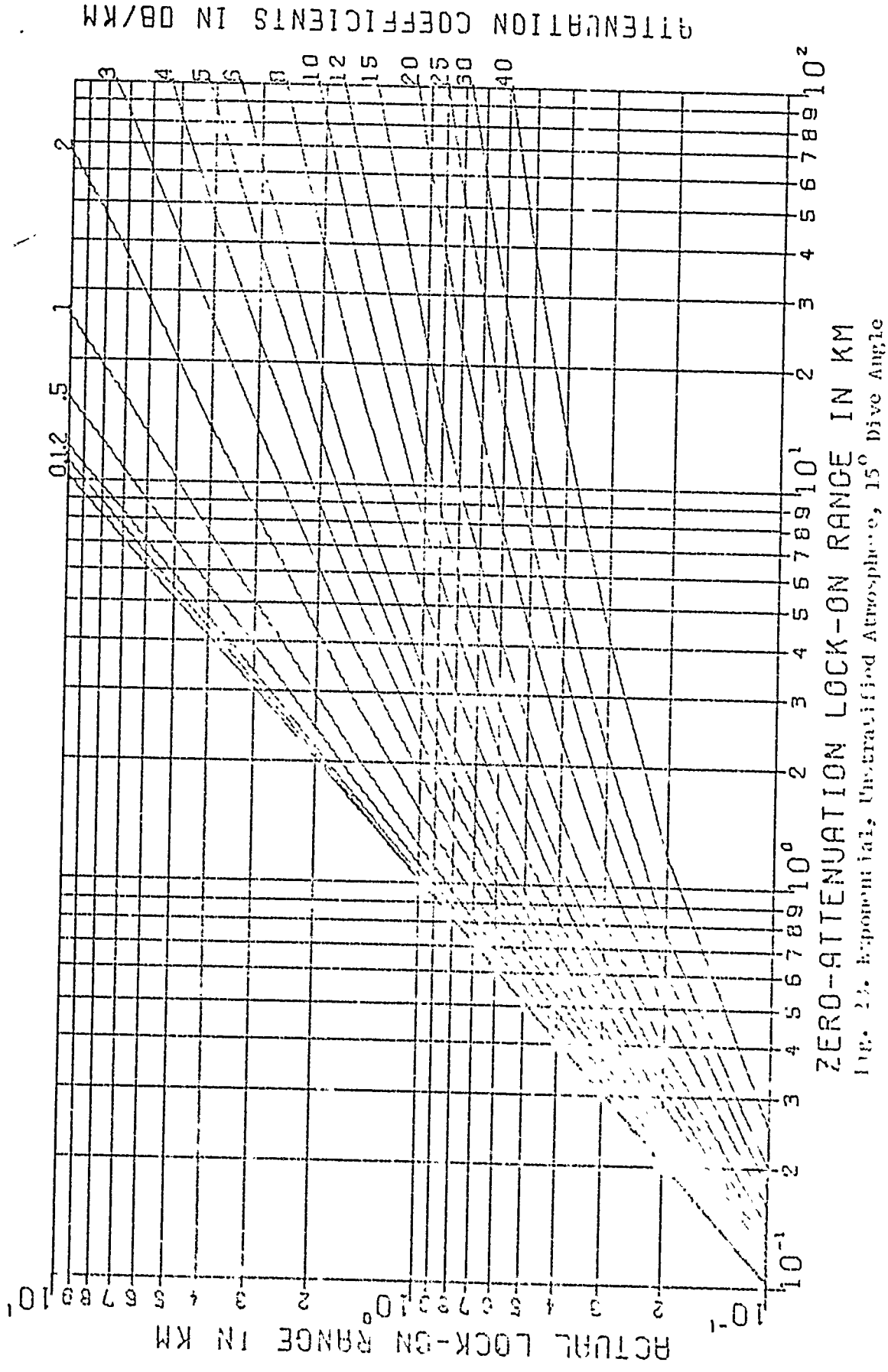

Fig. 22. Exponential, Uncrarified Atmosphere, 15° Dive Angle

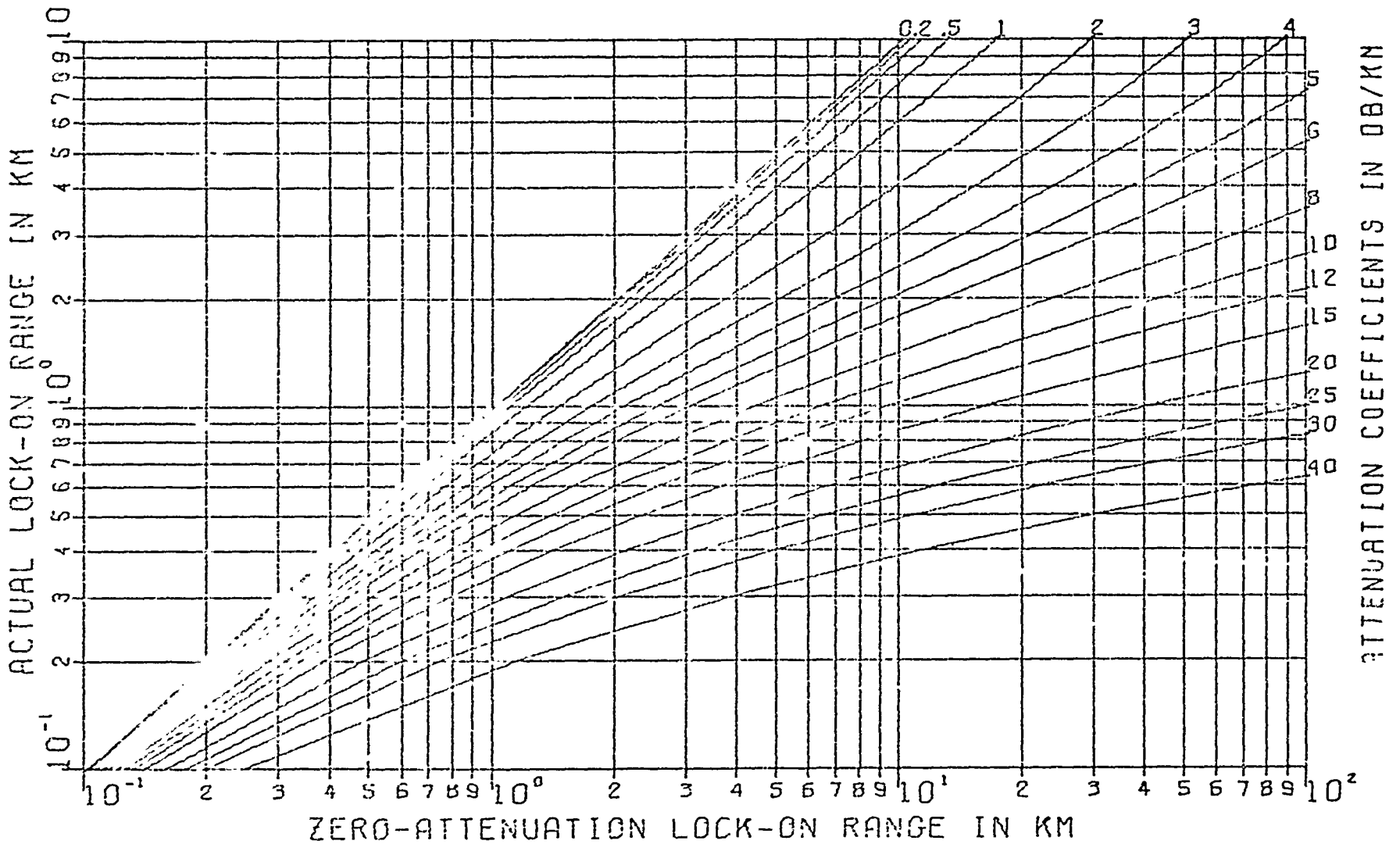

Fig. 24. Exponential, Untratified Atmosphere, 30^{O} Dive Angle

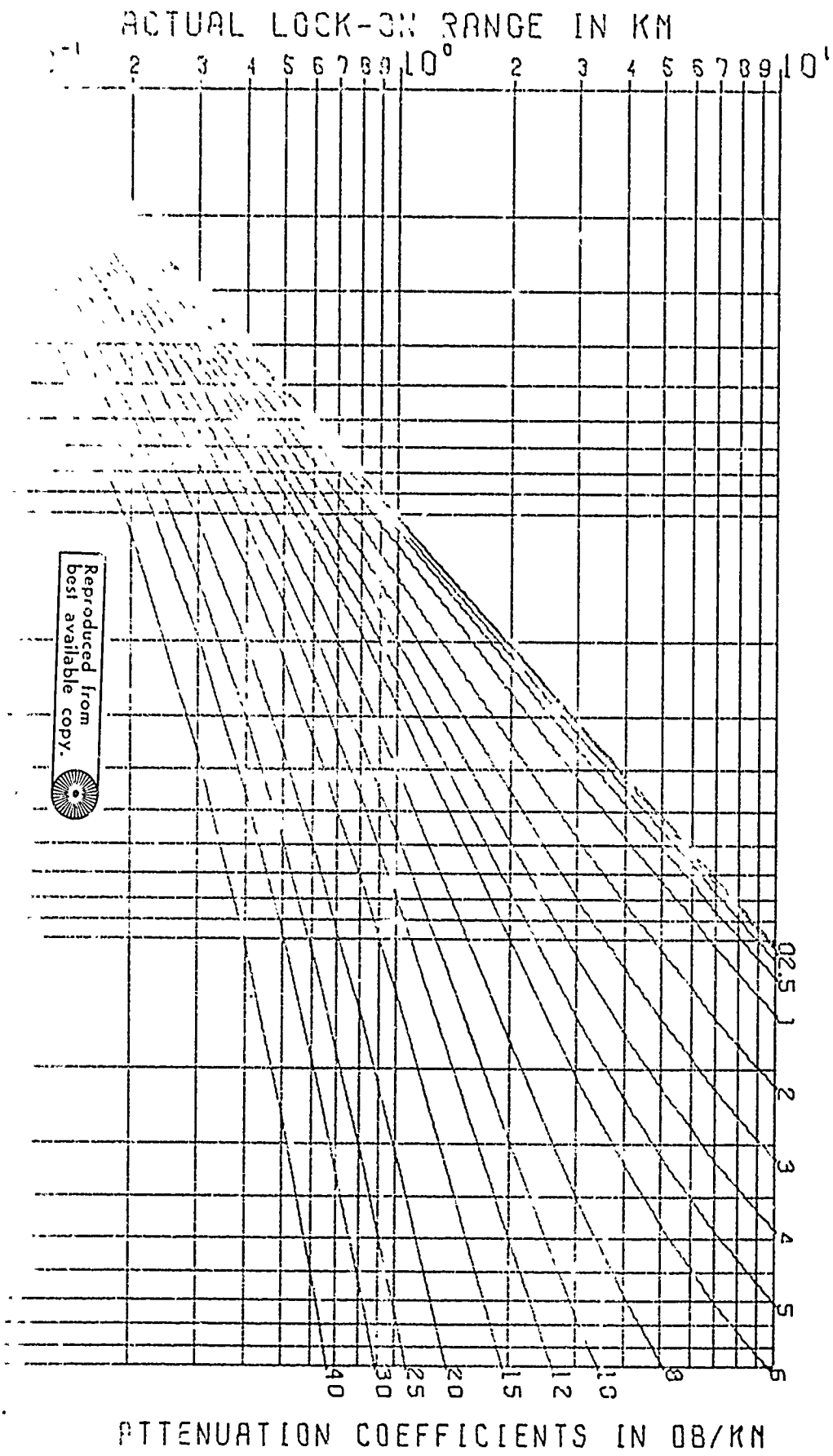

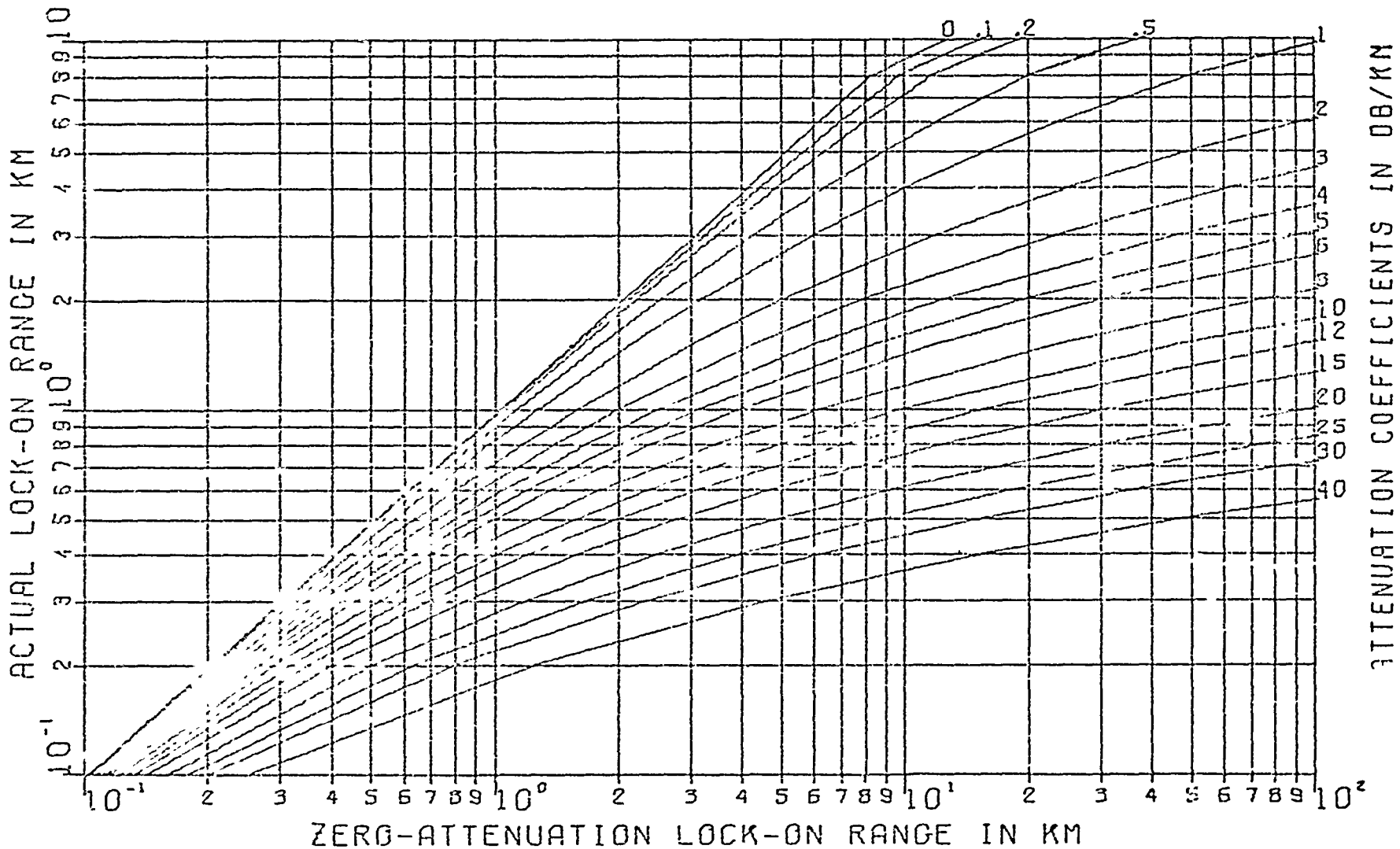

Fig. 2c. Stratified Atmosphere, Three Homogeneous Layers, 10° Dive Angle

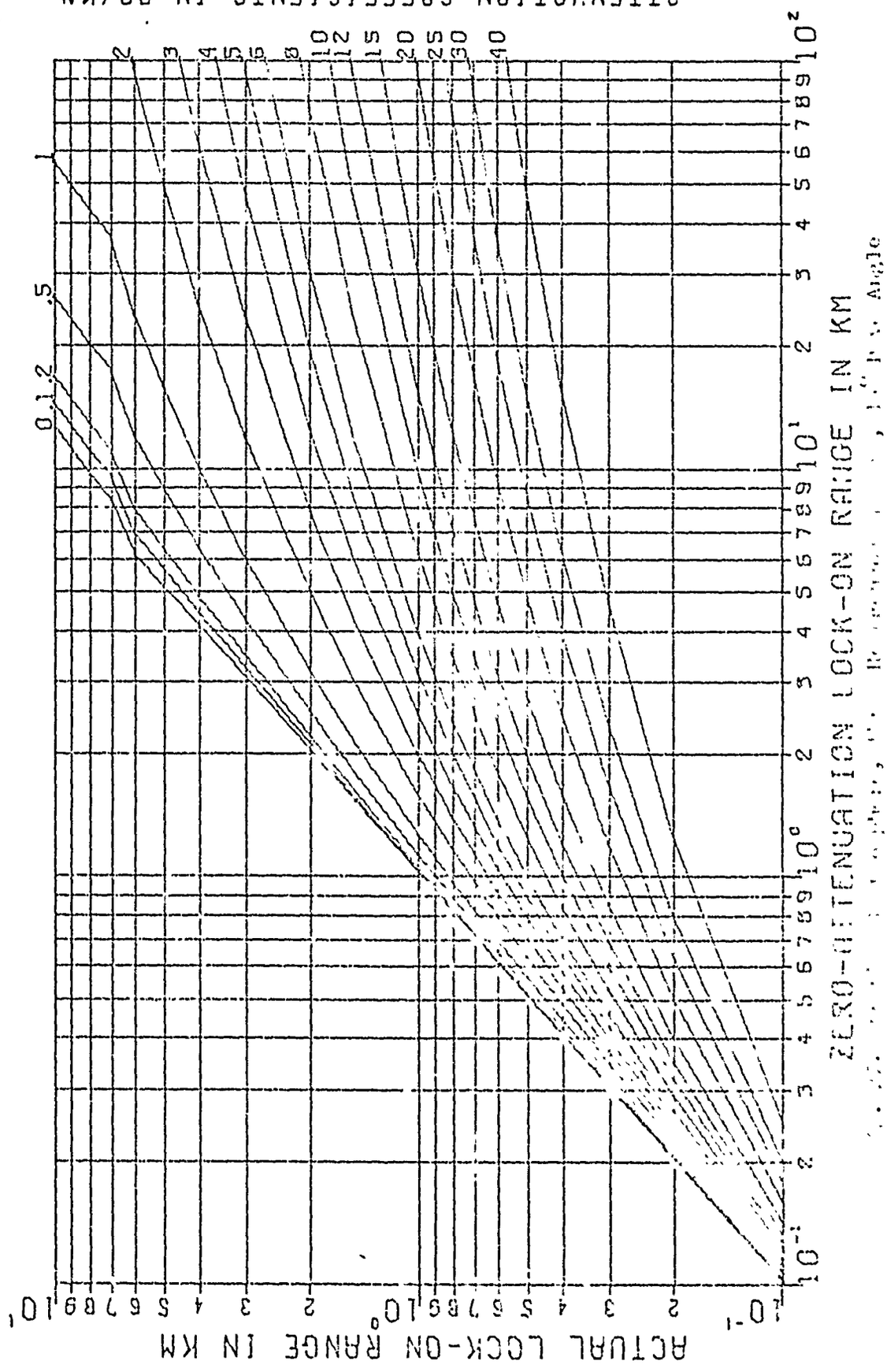
ATTENUATION COEFFICIENTS IN DB/KM
2 3 4 5 6 8 10 12 15 20 25 30 40
1 .5 0.1.2
ZERO-ATTENUATION LOCK-ON RANGE IN KM
ACTUAL LOCK-ON RANGE IN KM

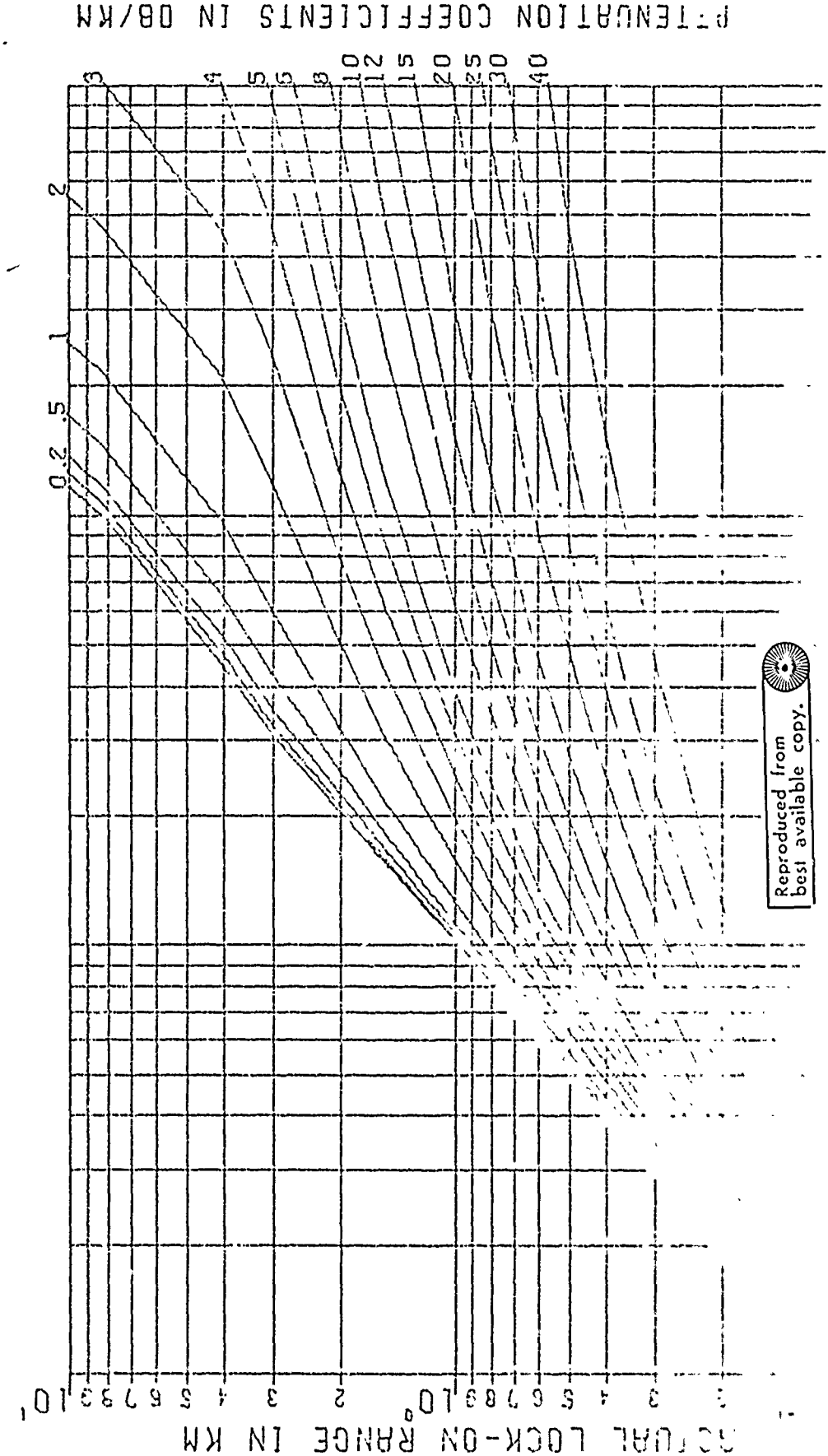
ATTENUATION COEFFICIENTS IN DB/KM
3
4
5
6
8
10
12
15
20
25
30
40
2
1
.5
0.2
ACTUAL LOCK-ON RANGE IN KM
10
10
Reproduced from
best available copy.

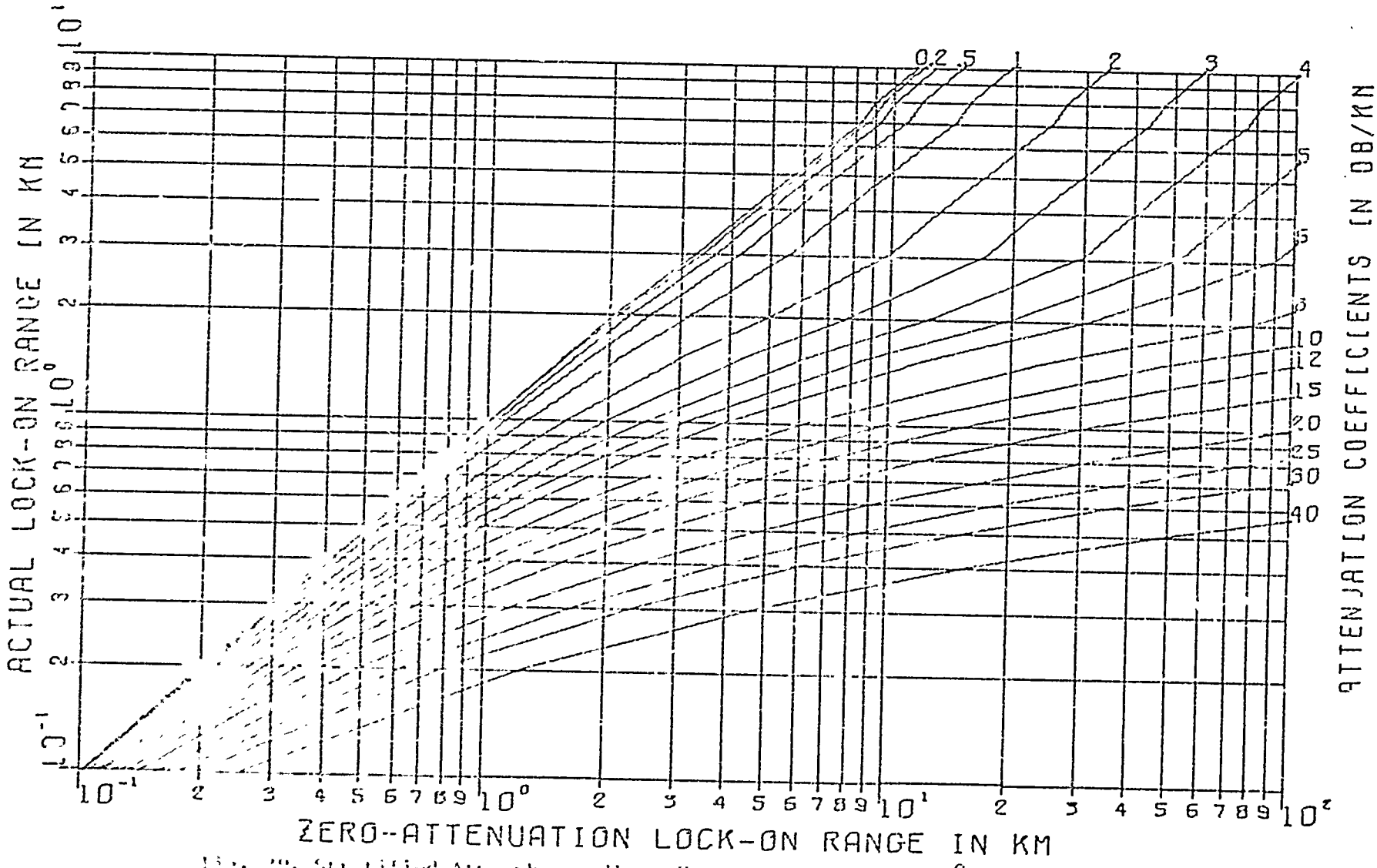

Fig. 20. Stratified Atmosphere, Three Homogeneous Layers, 45° Dive Angle

Appendix D

Computation of Attenuation Coefficients

If I_1 = intensity received at near distance R_1, I_2 = intensity received at far distance R_2, and β = attenuation coefficient in dB/unit length of R_1 & R_2 in the experiment in Chapter V, then:

$$I_1 = \frac{I_o}{R_1^2} 10^{-\left[\frac{\beta R_1}{10}\right]} \quad , \text{ or } I_o = I_1 R_1^2 \, 10^{+\left[\frac{\beta R_1}{10}\right]} \tag{59}$$

$$I_2 = \frac{I_o}{R_2^2} 10^{-\left[\frac{\beta R_2}{10}\right]} \quad , \text{ or } I_o = I_2 R_2^2 \, 10^{+\left[\frac{\beta R_2}{10}\right]}. \tag{60}$$

Therefore:

$$I_1 R_1^2 \, 10^{\left[\frac{\beta R_1}{10}\right]} = I_2 R_2^2 10^{\left[\frac{\beta R_2}{10}\right]} \quad , \text{ or } 10^{\beta(R_2 - R_1)/10} = \frac{I_1 R_1^2}{I_2 R_2^2} \tag{61}$$

And:

$$\beta = \frac{10}{(R_2 - R_1)} \log_{10} \left[\frac{I_1}{I_2}\right]\left[\frac{R_1}{R_2}\right]^2 \tag{48}$$

For small $\Delta\beta$, ΔI_1, ΔI_2: $\Delta\beta = \frac{\partial\beta}{\partial I_1}\Delta I_1 - \frac{\partial\beta}{\partial I_2}\Delta I_2$ (62)

The negative sign of the second term is necessary because ΔI_1 and ΔI_2 have opposite effects; an increase in I_1 alone will increase β, but an increase in I_2 alone will decrease β.

The relationship between β and visibility is as follows. The true meteorological range (true visibility) is the range at which contrast is reduced to 2% (note some countries use 5%), or:

$$0.02 = 10^{-\beta V/10} \quad , \text{ or } \beta V = 10 \log_{10} 50 = 17.0 \quad \text{or } \beta = \frac{17.0}{V_{true}} \tag{37}$$

Vita

James Vernon Mardis was born on 1 January 1943 in Logan, Utah. Raised near San Diego, he graduated from Helix High School in 1960 and San Diego State University in 1965, receiving a Bachelor of Science degree in Nuclear Physics and a commission in the USAF. He graduated from pilot training at Laredo and instructor pilot training at San Antonio in 1966. He served as an instructor pilot for four years, at Reese AFB, Texas, and Columbus AFB, Mississippi. He is attending the Air Force Institute of Technology where he is working on the degree of Master of Science in Engineering Physics in 1972. His civilian scientific employment includes full-time and part-time positions as a technician, research engineer, and research scientist for the US Navy Electronics Laboratory, San Diego; the Astronomy Department and the Physics Department of San Diego State University; and Ryan Electronics Division of Ryan Aeronautics Corporation.

Permanent address: 226 Briarcroft Rd, Claremont, Calif. 91711.